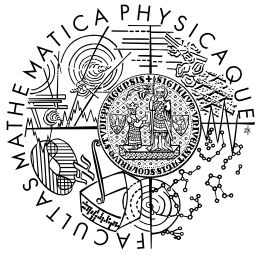

FACULTY
OF MATHEMATICS
AND PHYSICS
Charles University

MASTER THESIS

Mgr. Bc. Dominik Vach

Surface manifestation of melting within the ice shell of Europa

Mathematical Institute of Charles University

Supervisor of the master thesis:	RNDr. Klára Kalousová Ph.D.
Study programme:	Matematical and Computational Modelling in Physics
Study branch:	Physics

Prague 2019

I declare that I carried out this master thesis independently, and only with the cited sources, literature and other professional sources.

I understand that my work relates to the rights and obligations under the Act No. 121/2000 Sb., the Copyright Act, as amended, in particular the fact that the Charles University has the right to conclude a license agreement on the use of this work as a school work pursuant to Section 60 subsection 1 of the Copyright Act.

In ..... date ..... signature of the author

The author is grateful especially to his supervisor, RNDr. Klára Kalousová, Ph.D. for her valuable comments and advice based on her excellent insight into the research topic which was crucial in pointing the thesis in the right direction. Further, the author is also very thankful to his family and friends, who supported and motivated him throughout his university studies.

Title: Surface manifestation of melting within the ice shell of Europa

Author: Mgr. Bc. Dominik Vach

Department: Mathematical Institute of Charles University

Supervisor: RNDr. Klára Kalousová Ph.D., Department of Geophysics

Abstract: One of the most interesting extraterrestrial bodies in the Solar System is Europa, the icy satellite of Jupiter. This icy moon might have a sufficiently hospitable environment which could be harbouring life in the subsurface ocean deep under its icy crust. The thesis thoroughly examines the generation process of one of the surface formations called chaotic terrains. These huge areas of ice disruptions which uniquely characterize Europa's surface might play a significant role in the understanding of the inner structure of the moon. The latest research assumes the chaotic terrains form above liquid water lenses perched relatively shallow in the ice shell, however, no numerical simulations have been performed to confirm this theory. The goal of the thesis is to create a model which would validate the theory and explain the formation process of the chaotic terrains. The thesis runs several simulations, and our results suggest these water lenses and the process in the mantle might play a key role in the chaotic terrains formation.

Keywords: Europa Melting Free Surface Plasticity

Název práce: Povrchová deformace jako důsledek tání v ledové slupce Europy

Autor: Mgr. Bc. Dominik Vach

Ústav: Matematický ústav Univerzity Karlovy

Vedoucí práce: RNDr. Klára Kalousová Ph.D., Katedra geofyziky

Abstrakt: Jedno z nejzajímavějších těles sluneční soustavy je Europa, ledový měsíc Jupiteru. Tento ledový měsíc by mohl mít dostatečně příznivé prostředí pro existenci forem života ve svém podpovrchovém oceánu hluboko pod ledovou slupkou. Tato práce zkoumá proces vzniku povrchových útvarů, které jsou nazývány chaotické terény. Tyto obrovské oblasti s narušenou strukturou povrchu, které jedinečně charakterizují povrch Europy, můžou hrát podstatnou roli v porozumění struktury a procesů uvnitř ledové slupky měsíce. Aktuální teorie předpokládají, že chaotické terény vznikají nad vodními rezervoáry umístěnými relativně blízko u povrchu v ledové slupce, nicméně tato hypotéza nebyla zatím ověřena numerickými simulacemi. Cílem této práce je navržení matematického modelu a spuštění simulací pro ověření této hypotézy. Výsledky práce ukazují, že existence vodních rezervoárů pod povrchem aspolečně s procesy uvnitř slupky mohou mít vliv na deformaci povrchu, a tak i vznik chaotických terénů.

Klíčová slova: Europa Tání Volný povrch Plasticita

Contents

Introduction

It has been almost 30 years since the launch of unmanned spacecraft Galileo, named after the discoverer of Jupiter's largest satellites. Although it took 6 years to enter Jupiter's orbit, it soon turned out the gains from the mission were going to be priceless. As the Galileo probe examined Jupiter and its system, many of its satellites could have been studied exhaustively and more precisely from the data collected during the flybys. Galileo and Cassini, the other spacecraft sent to Saturn soon after Galileo, have discovered an exciting world of icy moons including Europa and Enceladus.

The obtained data indicate that these icy moons harbour huge subsurface oceans comprised of liquid water. Such finding then naturally raised a question of what is the source of the energy enabling the existence of the water in the liquid state under the ice shell. In case of Europa, the main sources of the energy are the tidal forces of Jupiter which generate enough energy to melt the ice and create vast water reservoirs that could potentially harbour some kind of life forms. Observations and findings like these only further stress the importance of understanding what are the icy moons comprised of and what processes are running under the ice shell.

As there are several hypotheses how the inner structure of the icy moons might look like, there is an urge to create a more rigorous mathematical model which would describe the underlying processes. In this thesis, the aim is to focus on the modelling of the processes occurring in the ice crust of Europa. One of the observed formations on the surface is so-called chaotic terrains. The terrains are characterized by ice disruption of Europa's surface into isolated plates which are connected to the rest of plates with a lumpy matrix material. These objects are unique in the Solar System and are of utmost importance for the understanding of Europa's internal processes. The correct model of the chaotic terrains formation might predict not only what is the inner structure of the icy satellite, but also how thick the layer of ice is and could improve the precision of the assumptions about the depth of the subsurface ocean and the overall material distribution beneath the surface. The chaotic terrains cover around one-quarter of Europa's surface and this makes them together with double ridges, the other specific formation on the surface, probably the most important objects, that might help to clarify the overall understanding of the icy moon formation and estimate the geological age of the surface.

The satellite images of plates in the chaotic terrains were thoroughly studied, and it was found out that they used to change their positions and rotate in the past. The scientists assumed several models considering melting of the ice shell via varying mechanisms based on this observation. The thesis aims to investigate the generation process of the chaotic terrains proposed by Schmidt et al. [2011] who suggest the chaotic terrains are a result of a four-phase melt-freezing mechanism.

The model by Schmidt et al. [2011] assumes that the formation process begins with a rising thermal plume from the subsurface ocean which approaches the eutectic point of the impure brittle ice, and hence, the melting process may start underneath the surface. The volumetric changes in the ice mantle cause ice fractures and these then result in the floating blocks of ice. After the thermal

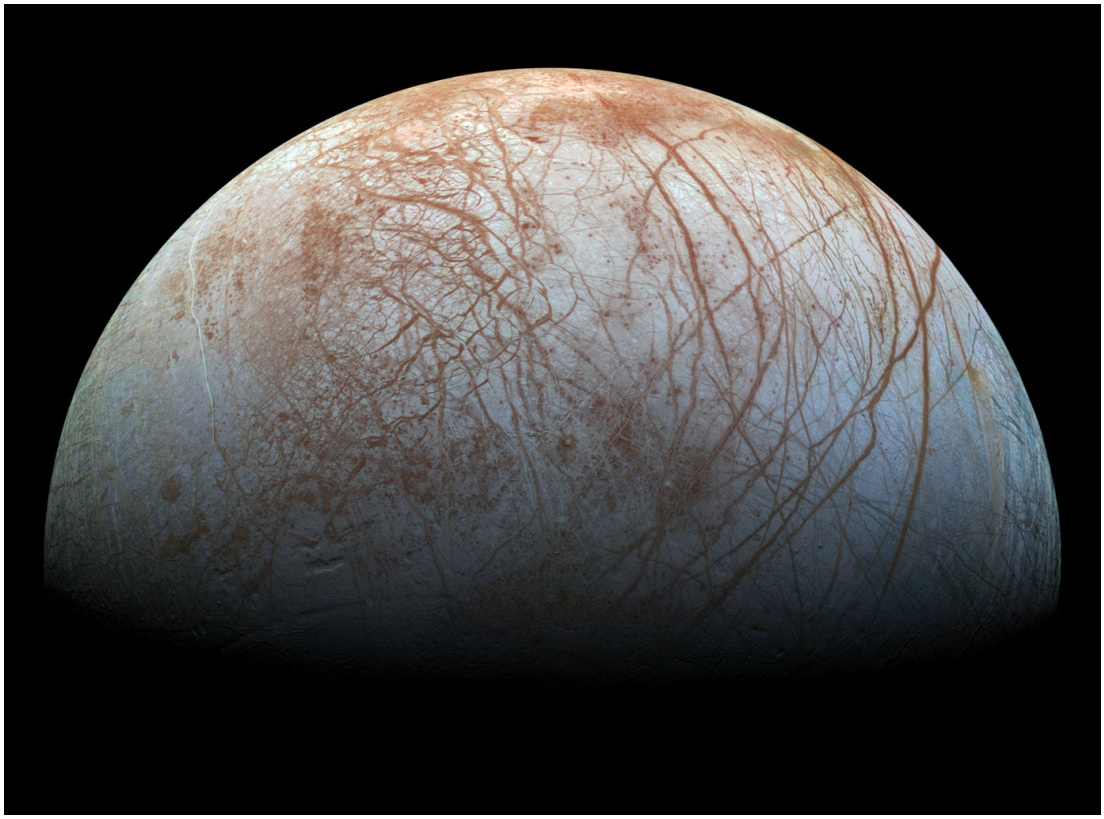

Figure 1: Europa's surface concealing a deep ocean of liquid water
Image courtesy of NASA/JPL/Ted Stryk

plume diminishes below this region, the surface starts to refreeze, which causes an increase of volume in the ice shell. In the end, this mechanism leads to the topographical changes on the Europa's surface, and the ice blocks are either standing above or below the surrounding terrain.

The thesis aims to validate this hypothesis by modelling and simulating the ice failure within the icy crust of the Europa's surface. In order to perform these simulations, a set numerical methods is used to model several phenomena that are known from other geophysical applications. Some of these phenomena were numerically modelled and tested by the geophysics community, therefore the thesis runs several benchmarks which should help to calibrate the final model.

The structure of the thesis is as follows: The first chapter is devoted to the motivation and literature review considering the space exploration and geophysical research. The second chapter introduces the mathematical formulation of the problem which this thesis aims to solve. In addition, it describes the mathematical framework and numerical methods used in the thesis to solve the final problem. The third chapter focuses on the individual features of numerical benchmarks and presents the results which are made in order to validate the model and numerical techniques used in the final model application. The fourth chapter is devoted to the final application simulation and presents the outcome of the thesis. The thesis is concluded by a discussion of the results.

1. Literature review

1.1 Motivation

Voyager probe images showed the first detailed recognition of the isolated patches that have been disrupted. The first name for the objects on the Europa's surface was "mottled terrain" which changed later and became dubbed "lenticulae" due to their shape. The initial ideas about the formation process of the uneven terrains supposed they were a result of a tectonic activity which was accompanied by the rise of the dark brown material from below. [Lucchitta and Soderblom, 1982]

This idea was alternated by Malin and Pieri [1986] who thought the mottled terrain is much older and has been subject to an exogenic change caused by an impact. Nevertheless, scientists came up with many more hypotheses for the Europa's surface features formation process soon after the Galileo probe collected high-quality images of the surface.

The terrains became quickly dubbed chaotic terrains due to their irregular shape and unclear formation process. Collins and Nimmo [2009] summarize the overview of formation hypotheses and present a synthesis of observations regarding the characteristics of the chaotic terrains, thus are followed in this chapter.

One of the most studied chaotic terrains on Europa is Conamara Chaos. This chaotic terrain has been well studied due to high-resolution images and became an archetype chaotic terrain due to its easily recognizable plates of ice which moved around, rotated, and tilted and had a key role in showing the evidence for a liquid subsurface ocean. This vast region of isolated plates made out of ice in an irregular surrounding lumpy matrix material is shown in detail in the Fig. 1.1 and a larger scale view on the ice blocks is depicted in the Fig. 1.2.

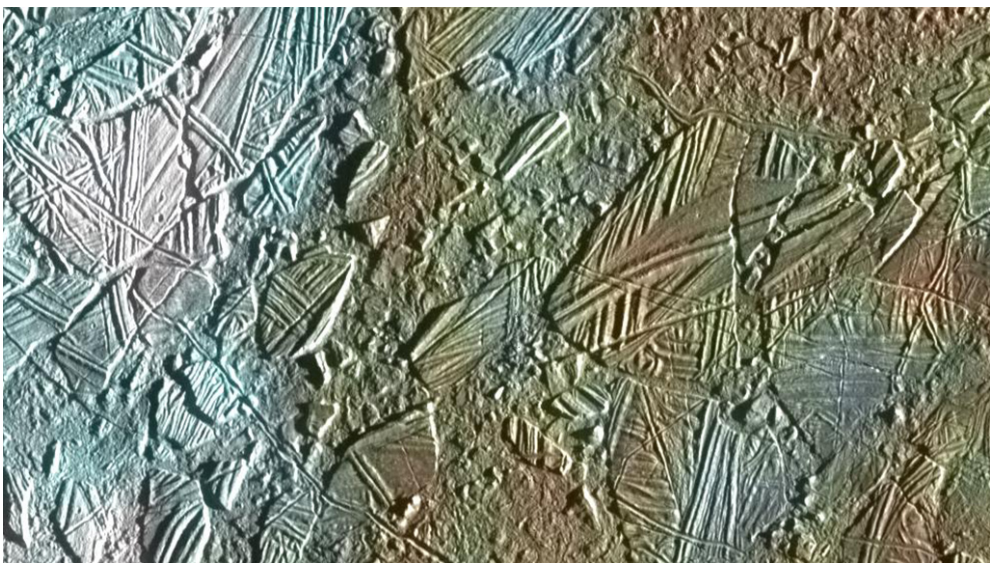

Figure 1.1: Detailed view of the ice blocks structure in Conamara Chaos
Image courtesy of NASA/JPL/University of Arizona

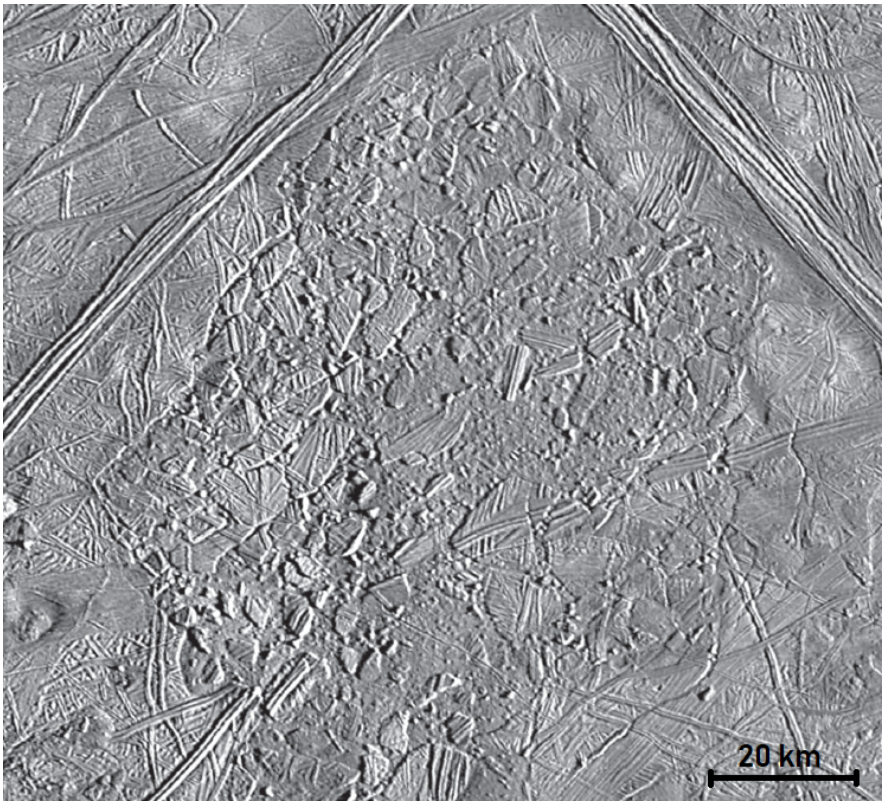

Figure 1.2: Europa's well known chaotic terrain Conamara Chaos
Image courtesy of NASA/JPL/University of Arizona

Williams and Greeley [1998] in their analysis of shadows inferred that the plates in the Conamara Chaos are on average standing approximately 40 to 150 meters above the surrounding surface. In contrast to this observation, the other chaotic terrains such as e.g. Thera Macula turned out to have sunken topography even up to 800 meters below the surrounding surface.

This led the researchers to propose several different formation processes based on various mechanisms. Collins and Nimmo [2009] present five distinct theories, and the thesis follows their description.

1.2 Chaotic terrains formation hypotheses

The first hypothesis follows the mechanisms known from Earth which assumes that the chaotic terrains emerge as a result of melting through the icy shell. However, this theory has a flaw - double ridges, the other surface formation, would melt faster and thus flatten the surface due to the thermal conduction through the ice and radiation of the energy into space. [Goodman et al., 2004] Moreover, the energy that needs to be delivered to the surface in order to produce and sustain melt of the icy shell would be too big. [Collins and Nimmo, 2009]

The second hypothesis suggests the chaotic terrains might be the result of diapirism - a geological process known from Earth, during which less dense material rises through buoyant forces. This process seems to plausibly explain some of the chaotic terrains with dome structure such as Murias Chaos and Thera Macula as shown e.g. by [Mével and Mercier, 2007]. Nevertheless, while this mechanism

might explain some of the chaotic terrains, the problem is that it requires a similar size of the diapirs as it depends on the thickness of the icy shell. This contradicts the variety of sizes of individual chaotic terrains, and thus does not offer a general process which would explain the formation of other chaotic terrains. [Collins and Nimmo, 2009]

The third hypothesis follows the possibility of brine mobilization. This approach assumes the composition of materials contained in the ice shell might significantly lower the ice viscosity if the shell is heated. This could allow the percolation of liquids through the layer if the added materials decreased the melting point of the ice composition. [Collins and Nimmo, 2009]

The fourth hypothesis relies on the injection of sills (i.e. the tabular intrusions in the geological material), directly from the ocean. This approach alone would be hard for the sills to propagate through the cracks in the ice without any additional energy. It was shown by Manga and Wang [2007] that the water could form sills below the surface within the ice shell. This model has not been, however, studied that rigorously as the other models as it is not as promising as the previous models. [Collins and Nimmo, 2009]

The last hypothesis points on the possibility of an exogenic impact which could penetrate the surface. This option was studied by Cox et al. [2005], who suggested the large scale chaotic terrains might be the result of an impact. However, this theory is contradicted by other crater examples on Europa's surface which did not cause the formation of the chaotic terrain and are surrounded by secondary craters and concentric fractures similarly to other bodies in the Solar System. [Collins and Nimmo, 2009]

Table 1.1 summarizes the hypotheses as presented in Collins and Nimmo [2009] and covers the information about the chaotic terrains, the advantages, and the disadvantages of particular hypotheses. The table is split to hard observational constraints that need to be satisfied by the model necessarily, and soft constraints that might be subject to misinterpretation or misclassification of the features.

Observational Constraint (H = hard constraint; S = soft constraint)	Melt Through	Diapirism	Brine Mobilization	Sill Injection	Impact
H1: Formation of matrix material	✓	✶	✓	×	✓
H2: Plates locally higher than matrix	✓	×	✓	×	✓
H3: Plates tilt, rotate, and translate	✓	✶	✶	✶	✓
H4: Nature of chaotic terrain margins	✶	✶	✶	×	✶
H5: Matrix topographically high	✶	✶	✓	✶	✶
H6: Dark hydrated salts/acid	✓	✶	✓	✓	✓
H7: Diameter range ~1–1000 km	✶	×	✶	✓	×
H8: Concentrated near the equator	✶	✶	✶	×	×
S1: Associated pits and domes	×	✓	✓	×	×
S2: Preexisting structures preserved	×	✓	✓	✓	×
S3: Plate size >1 km	✓	×	✶	✶	✓
S4: Ridges preferentially preserved	✓	✶	✶	✶	×
S5: Matrix material forms viscous flows	×	✓	✓	✶	✶
S6: Associated domes ~1 km high	×	✶	✶	✶	×
S7: Chaos regions grow by merging	✶	✓	✓	✓	×
S8: Matrix formation long-lived?	×	✶	✶	✶	×

Symbols: ✓ = This model naturally explains this observation. ✶ = Special, but plausible, circumstances may be required to produce this observation from this model. × = This model does not plausibly explain this observation.

Table 1.1: Comparison of hypotheses for chaotic terrains formation
Source: Collins and Nimmo [2009]

The authors of the paper summarizing the hypotheses favourize the melting through the icy shell and brine mobilization as these mechanisms are able to fulfill the hard observational constraints. Nevertheless, some of the soft constraints are not plausible or could be acceptable only in special cases. These flaws of the presented five mechanisms eventually led Schmidt et al. [2011] to the four-phase water lenses model.

Schmidt et al. [2011] mention that the melt-through of the ice shell is thermodynamically improbable, and the buoyancy of material rising in diapirs is not big enough to create the chaos heights. The motivation for their hypothesis comes from the subglacial volcanoes on Earth and analysis of data from Europa. Their idea is to model the formation of the chaotic terrains by supposing the existence of subsurface water lens-shaped lake in the ice shell.

Their hypothesis focuses on explaining the Conamara Chaos and Thera Macula formation where the former is raised above the surface whereas the latter is sunken below the surface. Thera Macula has a special role as the researchers claim the area is actively resurfacing and thus the formation process has not ended yet. A detailed view of Thera Macula is depicted in Fig. 1.3 with edited colours where the purple end of the colour range depicts sunken topography and the red end of the colour range depicts the raised topography. The schema depicting the whole process for the proposed four-phase "lens-collapse model" is available in Fig. 1.4.

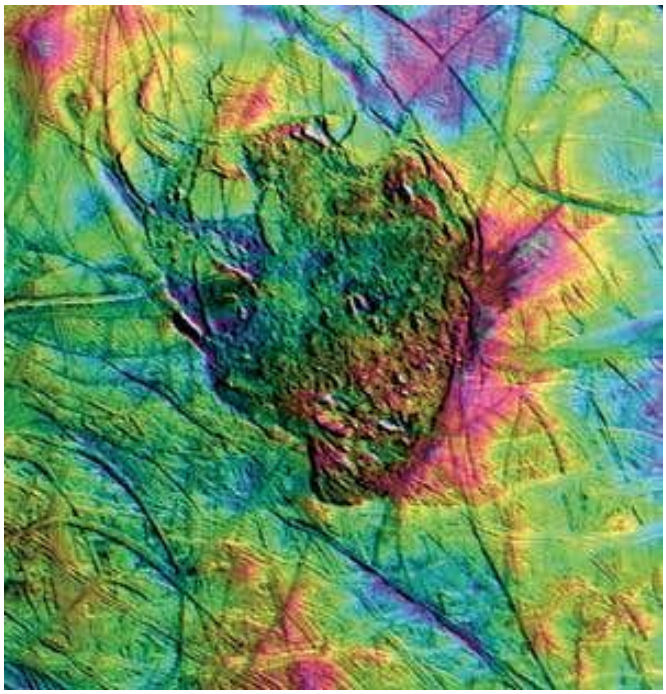

Figure 1.3: The sunken topography of Thera Macula chaotic terrain
Image courtesy of NASA/JPL, Source: Schmidt et al. [2011]

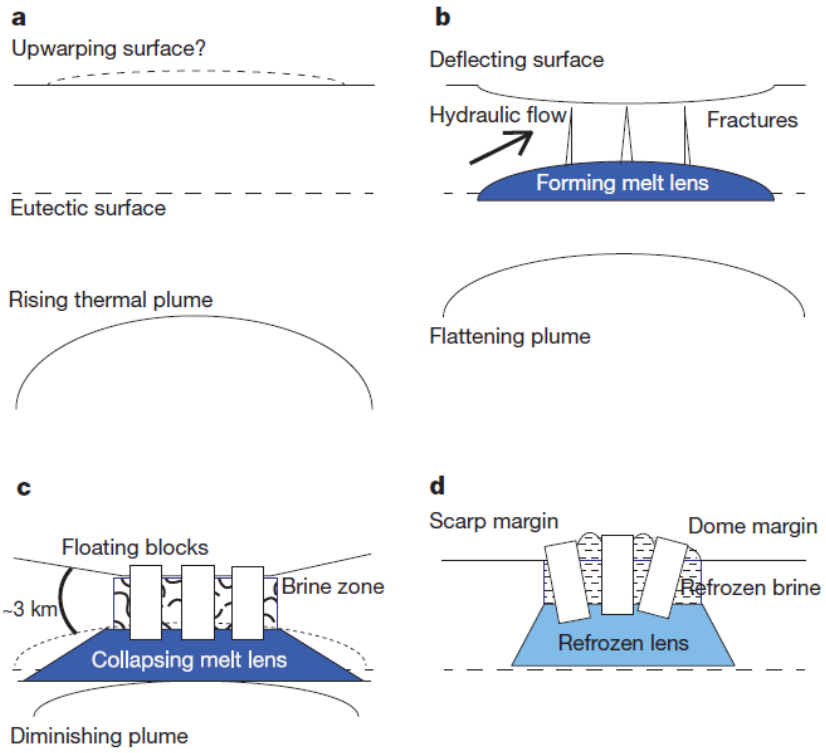

Figure 1.4: The four-phase "lens-collapse model" schema
Source: Schmidt et al. [2011]

The process starts with a rising thermal plume from the subsurface ocean. As the plume reaches the eutectic point of the impure ice (i.e. the material starts to melt due to the presence of salts), the ice starts to melt and consequently creates a subsurface lake. The overall volume in the region diminishes due to the melting process which causes a tension on the surrounding material.

The increasing pressure in the material results in cracking of the ice layer above the water lens. The cracks create floating blocks of ice that might move and rotate. In this phase, these floating blocks are sunken below the surrounding topography due to the volumetric changes in the region.

In the next phase, as the thermal plume starts to diminish, the subsurface lake gradually cools down, which eventually leads to refreezing of the perched water lens. As long as the subsurface area refreezes, the floating ice blocks are raising upwards and pushed by the increasing volume in the region.

The last phase of the model assumes that the blocks are standing above the surrounding surface and form the regions of ice blocks refreezed into fully frozen surface. This process suggests that Conamara Chaos is already a result of the forming process whereas chaos terrains such as Thera Macula are still actively forming above a subsurface lake under the influence of a rising thermal plume. [Schmidt et al., 2011]

2. Theoretical part

The aim of this chapter is to provide a theoretical framework for the mathematical problem solved in this thesis. The chaotic terrains formation is a key process in the understanding of the processes in the Europa's icy shell, and thus the thesis follows the four-phase lens collapse hypothesis suggested by Schmidt et al. [2011], which was introduced in chapter 1. The numerical implementation of the model faces several obstacles and therefore this chapter aims to provide the necessary description of mathematical relationships and numerical tools used in the thesis.

2.1 Problem setup

2.1.1 Governing equations

The goal of the thesis is to present a mathematical model which is able to reconstruct the processes in Europa's ice shell leading to a chaotic terrain formation. The chosen setup focuses on the formation of the sunken chaotic terrain which means that the model assumes volumetric decrease caused by the melting in the subsurface area. The mathematical model is given by the following governing equations

$$\nabla \cdot \vec{v} = \frac{\rho_{ice} - \rho_{water}}{\rho_{ice}\rho_{water}}\gamma, \tag{2.1}$$

$$-\nabla p + \nabla \cdot \boldsymbol{\sigma} + \rho_{ice}\vec{g} = \vec{0}, \tag{2.2}$$

$$\frac{\partial \boldsymbol{\epsilon}_p^{II}}{\partial t} + \vec{v} \cdot \nabla \boldsymbol{\epsilon}_p^{II} = \dot{\boldsymbol{\epsilon}}_p^{II}, \tag{2.3}$$

where $\vec{v}$ is the velocity, $\rho_{ice} = 920kg \cdot m^{-3}$ is the density of ice and $\rho_{water} = 1000kg{\cdot}m^{-3}$ is the density of water, γ is the melt production rate, p is the pressure, $\boldsymbol{\sigma}$ is the deviatoric part of the Cauchy stress tensor $\boldsymbol{\tau}$, g is the gravitational acceleration, $\boldsymbol{\epsilon}_p$ is the plastic strain, $\dot{\boldsymbol{\epsilon}}_p$ is the plastic strain rate, and throughout the thesis all tensors $\mathbb{A}$ with the superscript $(\cdot)^{II}$ are second invariants of the tensors defined as $\mathbb{A}^{II} = \sqrt{\frac{1}{2}\mathbb{A} : \mathbb{A}}$.

The first equation (Eq. 2.1) in the solved system of partial differential equations is the continuity equation which models an incompressible fluid in the domain Ω with the feature of volumetric change due to the melting of the material in the molten region corresponding to the water lens. The reasoning behind the melt production term in the continuity equation follows from the model used in Kalousová et al. [2016].

The second equation (Eq. 2.2) is the balance of momentum where the deviatoric part of the Cauchy stress tensor is defined as

$$\boldsymbol{\sigma} = 2\eta_{eff}\dot{\boldsymbol{\epsilon}} = 2\eta_v\dot{\boldsymbol{\epsilon}}_v = 2\eta_p\dot{\boldsymbol{\epsilon}}_p, \tag{2.4}$$

where η_v is the viscous part of viscosity, η_p is the plastic part of viscosity, η_{eff} is the effective viscosity, $\dot{\boldsymbol{\epsilon}}$ is the strain rate defined as $\dot{\boldsymbol{\epsilon}} = \frac{1}{2}(\nabla\vec{v} + (\nabla\vec{v})^T)$ and

consists of viscous $\dot{\boldsymbol{\epsilon}}_v$ and plastic part $\dot{\boldsymbol{\epsilon}}_p$:

$$\dot{\boldsymbol{\epsilon}} = \dot{\boldsymbol{\epsilon}}_v + \dot{\boldsymbol{\epsilon}}_p. \tag{2.5}$$

The relationship for the effective viscosity follows from the Eqs. (2.4) and (2.5)

$$\eta_{eff} = \left(\frac{1}{\eta_v} + \frac{1}{\eta_p} \right)^{-1}. \tag{2.6}$$

The viscous part of the effective viscosity is dependent on the temperature field T and therefore follows the exponential form from Showman and Han [2004]

$$\eta_v(T) = \eta_0 e^{\frac{Q}{R}(\frac{1}{T} - \frac{1}{T_0})}, \tag{2.7}$$

where $Q = 5 \cdot 10^4 J \cdot mol^{-1}$ is the activation energy for the creep process, $R = 8.314 J \cdot K^{-1} \cdot mol^{-1}$ is the gas constant, and $T_0 = 270K$ is the reference temperature which corresponds to the viscosity parameter $\eta_0 = 10^{16} Pa \cdot s$. The plastic part of the effective viscosity is defined as

$$\eta_p = \frac{\sigma_Y(p, C, \phi)}{2\dot{\epsilon}^{II}}, \tag{2.8}$$

which is dependent on the yield stress σ_Y. σ_Y is a function of pressure p, cohesion C and the angle of internal friction ϕ described in more detail in section 2.2.4.

The last equation of the system (Eq. 2.3) is the plastic strain advection equation which yields the second invariant of plastic strain rate integrated along the material trajectory, and follows Maierová [2012] and Di Pietro et al. [2006].

The final model does not involve the heat transfer equation for the sake of simplicity and assumes the temperature field T constant in time, however, several benchmarks done in the thesis substitute the plastic strain advection equation (2.3) for the heat transfer equation in the following form

$$\frac{\partial T}{\partial t} + \vec{v} \cdot \nabla T = \nabla^2 T, \tag{2.9}$$

where T is the temperature and t is the time.

2.1.2 Problem geometry

The governing equations are solved in the domain Ω which is $l = 60km$ wide and $h = 30km$ high and includes a partially molten region as shown in the Fig. 2.1 corresponding to the subsurface lake in the four-phase model by Schmidt et al. [2011]. The partially molten region is not distinguished as a special subset of Ω because the transition between the partially molten region and the rest of the domain Ω is smooth.

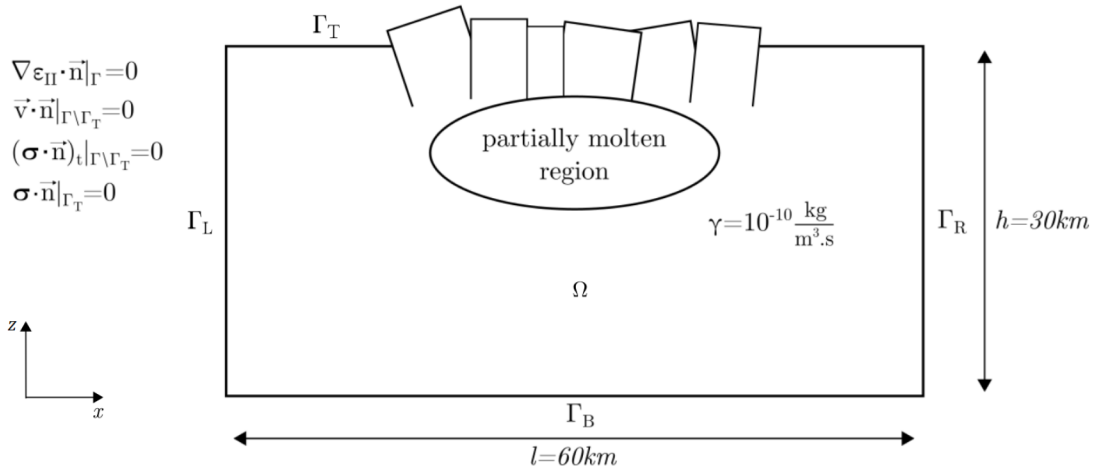

Figure 2.1: A schema of the problem geometry for the thermal convection benchmark

The figure also depicts the boundary conditions that hold at the boundary of the Ω domain $\Gamma = \partial\Omega$ and thus finish the problem specification. There is a free surface boundary condition on the top boundary Γ_T which is defined by $\boldsymbol{\sigma}\cdot\vec{n} = 0$, where $\vec{n}$ is the normal vector to the boundary oriented outwards from the domain Ω. On the remaining boundaries $\Gamma \setminus \Gamma_T$, there is a free-slip condition fulfilling no material inflow at the boundaries $\vec{v}\cdot\vec{n} = 0$ and no friction at the boundaries $(\boldsymbol{\sigma}\cdot\vec{n})_t = 0$, where the subscript t means the tangent component of resulting traction $\boldsymbol{\sigma}\cdot\vec{n}$. Last but not least, the model assumes no outflow and inflow at the boundaries, i.e. there is Neumann boundary condition prescribed as $\nabla\boldsymbol{\epsilon}^{II}\cdot\vec{n} = 0$ on Γ.

The spatial distribution of the melt production function γ follows the Gaussian functional form definition

$$\gamma(x,z) = \gamma_0 e^{-\left(\frac{x-x_0}{\Delta x}\right)^2-\left(\frac{z-z_0}{\Delta z}\right)^2}, \tag{2.10}$$

where $\gamma_0 = 10^{-10}$ is the amplitude parameter, x and z are the spatial coordinates (horizontal, vertical), $x_0 = 30000km$ and $z_0 = 23800km$ are the coordinates of the partially molten region centre, $\Delta x = 5500km$ and $\Delta z = 3200km$ are parameters influencing the size of the Gaussian peak in x and z direction, respectively. The partially molten region is also modified by the prescribed temperature field T where the temperature field reaches $T_{region} = 230K$ whereas out of the region the temperature grows linearly with the depth from $T_{min} = 100K$ at the top boundary to $T_{max} = 270K$ at the bottom boundary. The temperature field, melt production field, and the values of the parameters correspond to the setup in Kalousová et al. [2016].

The melting rate γ of the material and temperature T are both prescribed constant in time and are depicted in the Fig. 2.2.

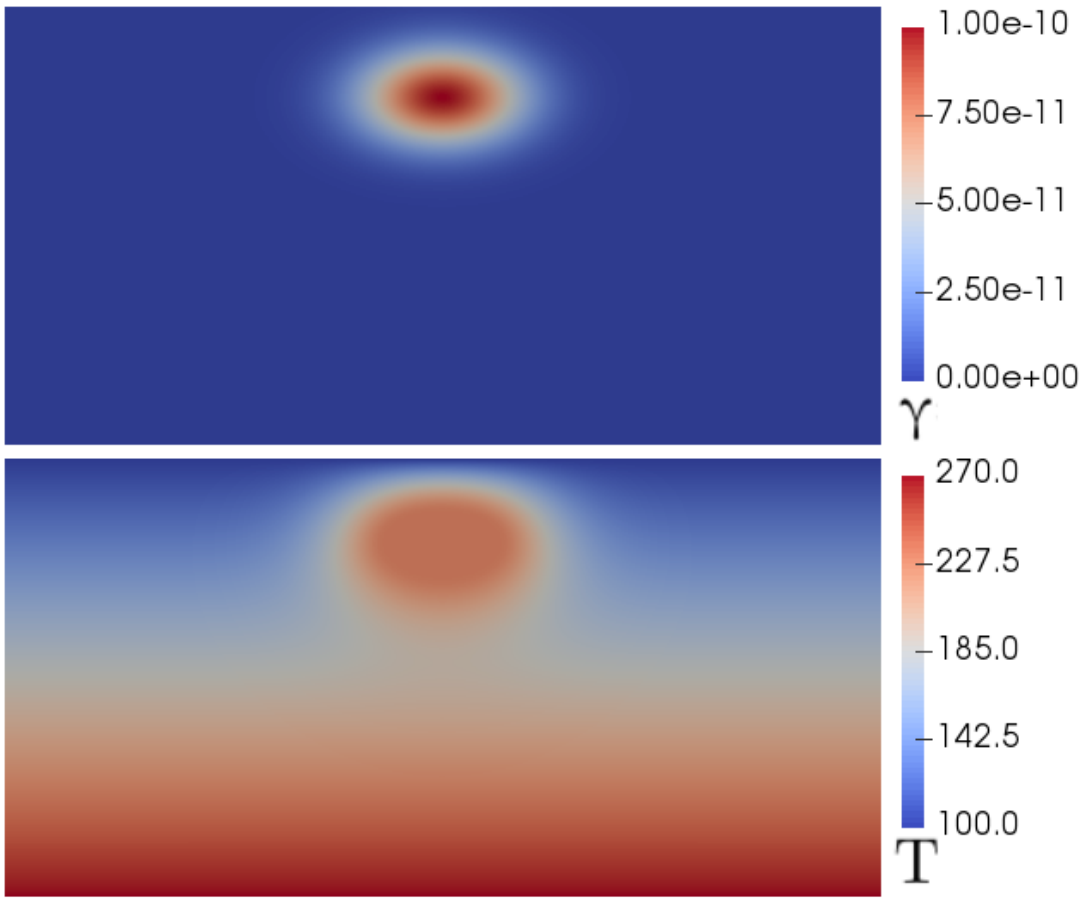

Figure 2.2: The scalar fields of melt production γ (above) and temperature T (below)

2.2 Mathematical framework

The aim of this section is to provide necessary mathematical background for the derivation of the governing equations (2.1),(2.2),(2.3) for the final problem and also for the benchmarks utilizing the heat transfer equation (2.9) in the thermal convection setup.

2.2.1 Fundamental balance laws of conservation

This subsection provides the balance laws in the form in which are used in geophysical applications. The balance laws are partial differential equations which describe the thermodynamical and mechanical interactions in the continuum mechanics. Their solution provides the time evolution of the spatially defined quantities of interest.

In order to derive them, two vector calculus results are needed. The thesis follows Matyska [2005] and Martinec [2003] both in the formulation of these results and the consequent balance laws derivation.

First, let us introduce modified Gauss divergence theorem. Consider a material volume $\Omega(t)$ with a boundary $\Gamma(t) = \partial\Omega(t)$ intersected by a moving singular

surface $\Sigma(t)$ (splitting the domain Ω, and thus generating the interface) across which a vector valued function $\vec{a}$ has a jump in values, then the Gauss theorem is expressed in the formula

$$\int_{\Gamma(t)\setminus\Sigma(t)} \vec{a}\cdot\vec{n}dS = \int_{\Omega(t)\setminus\Sigma(t)} \nabla\cdot\vec{a}dV + \int_{\Sigma(t)} [\![\vec{a}]\!]\cdot\vec{n}dS, \tag{2.11}$$

where $\vec{a}$ is an arbitrary continuously differentiable vector valued function (the relationship holds also for tensors) and $[\![\vec{a}]\!] = \vec{a}^{+} - \vec{a}^{-}$ is a jump in the value across the surface $\Sigma(t)$ obtained by subtracting the value on the negative side from the value on the positive side.

Consequently, the Reynolds transport theorem for a scalar quantity f is written as

$$\frac{D}{Dt}\int_{\Omega(t)} f dV = \int_{\Omega(t)\setminus\Sigma(t)} \left(\frac{\partial f}{\partial t} + \nabla\cdot(f\vec{v})\right) dV + \int_{\Sigma(t)} [\![f(\vec{v}-\vec{w})]\!]\cdot\vec{n}dS, \tag{2.12}$$

where $\frac{D}{Dt}$ is the material time derivative operator defined as $\frac{D}{Dt} := \frac{\partial}{\partial t} + (v\cdot\nabla)$, $\vec{v}$ is the particle velocity, $\vec{w}$ is the velocity of the interface which may be, in general, different from the particle velocity. f and $\vec{v}$ are required to be continuously differentiable at $\Omega(t)\setminus\Sigma(t)$. [Matyska, 2005]

The first balance law, the balance of mass, can be written as

$$\frac{D}{Dt}\int_{\Omega(t)} \rho dV = 0, \tag{2.13}$$

since there is no mass flow through the boundary. If we substitute the Reynolds transport theorem (2.12) into Eq. (2.13), we obtain

$$\int_{\Omega(t)\setminus\Sigma(t)} \left(\frac{\partial \rho}{\partial t} + \nabla\cdot(\rho\vec{v})\right) dV + \int_{\Sigma(t)} [\![\rho(\vec{v}-\vec{w})]\!]\cdot\vec{n}dS = 0, \tag{2.14}$$

which holds for any arbitrary volume $\Omega(t)$ (defined by its boundary $\Gamma(t)$), hence both integrands must be equal to zero locally

$$\frac{\partial \rho}{\partial t} + \nabla\cdot(\rho\vec{v}) = 0 \text{ in } \Omega(t)\setminus\Sigma(t), \tag{2.15}$$

$$[\![\rho(\vec{v}-\vec{w})]\!]\cdot\vec{n} \text{ in } \Omega(t)\setminus\Sigma(t). \tag{2.16}$$

If we use the result of Eq. (2.15) again in the Reynolds transport theorem Eq. (2.12), we obtain a useful formula

$$\begin{aligned}
\frac{D}{Dt}\int_{\Omega(t)} \rho f dV &= \int_{\Omega(t)\setminus\Sigma(t)} \left(\frac{\partial(\rho f)}{\partial t} + \nabla\cdot(\rho f\vec{v})\right) dV + \int_{\Sigma(t)} [\![\rho f(\vec{v}-\vec{w})]\!]\cdot\vec{n}dS = \\
&= \int_{\Omega(t)\setminus\Sigma(t)} \left(\rho\frac{\partial f}{\partial t} + \rho\vec{v}\cdot\nabla f\right) dV + \left(f\left(\frac{\partial \rho}{\partial t} + \nabla\cdot(\rho\vec{v})\right)\right) dV \\
&+ \int_{\Sigma(t)} [\![\rho f(\vec{v}-\vec{w})]\!]\cdot\vec{n}dS = \\
&= \int_{\Omega(t)\setminus\Sigma(t)} \rho\frac{Df}{Dt} dV + \int_{\Sigma(t)} [\![\rho f(\vec{v}-\vec{w})]\!]\cdot\vec{n}dS.
\end{aligned} \tag{2.17}$$

The second balance law is the balance of linear momentum which represents the balance between the change of momentum (left-hand side of the equation) and acting forces (right-hand side of the equation) including the gravity, Coriolis, and centrifugal forces, and the forces corresponding to the surface tractions. The other body forces except the named ones are neglected. This balance law has the following form

$$\begin{aligned}\frac{D}{Dt}\int_{\Omega(t)}\rho\vec{v}dV = \int_{\Omega(t)}\rho\vec{g}dV - 2\int_{\Omega(t)}\rho\vec{\omega}\times\vec{v}dV \\ -\int_{\Omega(t)}\rho\vec{\omega}\times(\vec{\omega}\times\vec{x})dV + \int_{\Gamma(t)}\boldsymbol{\tau}\cdot\vec{n}dS,\end{aligned} \tag{2.18}$$

where $\vec{g}$ is the gravity acceleration, $\vec{\omega}$ is the angular frequency of the planet's rotation, $\vec{x}$ is the position vector, and $\times$ denotes the vector product. The application of Eq. (2.17) and Gauss theorem (2.11) on the Eq. (2.18) gets

$$\begin{aligned}&\int_{\Omega(t)\setminus\Sigma(t)}\left(\rho\frac{D\vec{v}}{Dt} - \rho\vec{g} + 2\rho\vec{\omega}\times\vec{v} + \rho\vec{\omega}\times(\vec{\omega}\times\vec{x}) - \nabla\cdot\boldsymbol{\tau}\right)dV \\ &+\int_{\Sigma(t)}[\![\rho\vec{v}(\vec{v}-\vec{w}) - \boldsymbol{\tau}]\!]\cdot\vec{n}dS = 0.\end{aligned} \tag{2.19}$$

The local principle used in case of balance of mass can be also applied to the Eq. (2.19)

$$\rho\frac{D\vec{v}}{Dt} = \rho\vec{g} - 2\rho\vec{\omega}\times\vec{v} - \rho\vec{\omega}\times(\vec{\omega}\times\vec{x}) + \nabla\cdot\boldsymbol{\tau} \text{ in } \Omega(t)\setminus\Sigma(t), \tag{2.20}$$

$$[\![\rho\vec{v}(\vec{v}-\vec{w}) - \boldsymbol{\tau}]\!]\cdot\vec{n} = 0 \text{ in } \Sigma(t). \tag{2.21}$$

The third balance law is the balance of angular momentum which can be obtained by taking vector product of the position vector on all integrands in the balance of linear momentum equation (2.18)

$$\begin{aligned}\frac{D}{Dt}\int_{\Omega(t)}\vec{x}\times\rho\vec{v}dV = \int_{\Omega(t)}\vec{x}\times\rho\vec{g}dV - 2\int_{\Omega(t)}\vec{x}\times(\rho\vec{\omega}\times\vec{v})dV \\ -\int_{\Omega(t)}\vec{x}\times(\rho\vec{\omega}\times(\vec{\omega}\times\vec{x}))dV + \int_{\Gamma(t)}\vec{x}\times(\boldsymbol{\tau}\cdot\vec{n})dS.\end{aligned} \tag{2.22}$$

Using the identities$\nabla\vec{x} = \mathbb{I}$, where $\mathbb{I}$ is an identity matrix, and $[\![\vec{x}]\!] = 0$, and the Eqs. (2.11), (2.17), (2.22) gives us

$$\begin{aligned}&\int_{\Omega(t)\setminus\Sigma(t)}\vec{x}\times\left(\rho\frac{D\vec{v}}{Dt} - \rho\vec{g} + 2\rho\vec{\omega}\times\vec{v} + \rho\vec{\omega}\times(\vec{\omega}\times\vec{x}) - \nabla\cdot\boldsymbol{\tau}\right)dV \\ &-\int_{\Omega(t)\setminus\Sigma(t)}\mathbb{I}\dot{\times}\boldsymbol{\tau}dV + \int_{\Sigma(t)}\vec{x}\times[\![\rho\vec{v}(\vec{v}-\vec{w}) - \boldsymbol{\tau}]\!]\cdot\vec{n}dS = 0,\end{aligned} \tag{2.23}$$

where $\dot{\times}$ is the double product consisting of vector and scalar products here defined as $\mathbb{I}\dot{\times}\boldsymbol{\tau} := \sum_{jk}\epsilon_{ijk}\delta_{jl}\tau_{kl}$, δ_{jl} is the Kronecker δ-symbol and ϵ_{ijk} is the

Levi-Civita permutation symbol. Due to the local principle in Eqs. (2.20) and (2.21), we obtain from the Eq. (2.23)

$$\mathbb{I}\dot{\times}\boldsymbol{\tau} = 0 \iff \boldsymbol{\tau} = \boldsymbol{\tau}^T, \tag{2.24}$$

where T stands for transposition. This means the implication of the balance of angular momentum is that the tensor $\boldsymbol{\tau}$ is symmetric.

The last balance law we are interested in in order to derive the governing equations is the balance of energy obtained by balancing the rate of work corresponding to the surface and body forces with the other sources of energy

$$\begin{aligned}\frac{D}{Dt}\int_{\Omega(t)}(\rho e + \frac{1}{2}\rho\vec{v}\cdot\vec{v})dV = &\int_{\Gamma(t)}\vec{v}\cdot\boldsymbol{\tau}\cdot\vec{n}dS + \int_{\Omega(t)}\rho\vec{g}\cdot\vec{v}dV \\ &-2\int_{\Omega(t)}\rho(\vec{\omega}\times\vec{v})\cdot\vec{v}dV - \int_{\Omega(t)}\rho(\vec{\omega}\times(\vec{\omega}\times\vec{x}))\cdot\vec{v}dV \\ &-\int_{\Gamma(t)}\vec{q}\cdot\vec{n}dS + \int_{\Omega(t)}HdV,\end{aligned} \tag{2.25}$$

where e is the internal energy per unit mass, $\vec{q}$ is the heat flow, and H denotes the heat sources per unit volume. The Coriolis forces cross out as the scalar product is zero due to perpendicularity of $\vec{v}$ and $\vec{\omega}\times\vec{v}$. The first integral on the right hand side of the previous equation can be rewritten as

$$\int_{\Gamma(t)}\vec{v}\cdot\boldsymbol{\tau}\cdot\vec{n}dS = \int_{\Omega(t)\setminus\Sigma(t)}\vec{v}\cdot(\nabla\cdot\boldsymbol{\tau}) + \nabla\vec{v} : \tau dV + \int_{\Sigma(t)}[\![\vec{v}\cdot\boldsymbol{\tau}]\!]\cdot\vec{n}dS, \tag{2.26}$$

where : denotes the double scalar product. If we substitute the local form of balance of linear momentum Eq. (2.20 into one of the integrals in Eq. 2.27), the following is obtained

$$\begin{aligned}\int_{\Omega(t)\setminus\Sigma(t)}\vec{v}\cdot(\nabla\cdot\boldsymbol{\tau})dV = &\int_{\Omega(t)\setminus\Sigma(t)}\frac{1}{2}\rho\frac{D}{Dt}(\vec{v}\cdot\vec{v})dV \\ &-\int_{\Omega(t)}\rho\vec{g}\cdot\vec{v}dV + \int_{\Omega(t)}\rho(\vec{\omega}\times(\vec{\omega}\times\vec{x}))\cdot\vec{v}dV.\end{aligned} \tag{2.27}$$

If we substitute Eqs. (2.26) and (2.27) back to (2.25), we obtain

$$\begin{aligned}\frac{D}{Dt}\int_{\Omega(t)}(\rho e + \frac{1}{2}\rho\vec{v}\cdot\vec{v})dV = &\int_{\Omega(t)\setminus\Sigma(t)}\frac{1}{2}\rho\frac{D}{Dt}(\vec{v}\cdot\vec{v})dV - \int_{\Omega(t)}\rho\vec{g}\cdot\vec{v}dV \\ &+\int_{\Omega(t)}\rho(\vec{\omega}\times(\vec{\omega}\times\vec{x}))\cdot\vec{v}dV + \int_{\Omega(t)\setminus\Sigma(t)}\nabla\vec{v} : \tau dV \\ &+\int_{\Sigma(t)}[\![\vec{v}\cdot\boldsymbol{\tau}]\!]\cdot\vec{n}dS + \int_{\Omega(t)}\rho\vec{g}\cdot\vec{v}dV - 2\int_{\Omega(t)}\rho(\vec{\omega}\times\vec{v})\cdot\vec{v}dV \\ &-\int_{\Omega(t)}\rho(\vec{\omega}\times(\vec{\omega}\times\vec{x}))\cdot\vec{v}dV - \int_{\Gamma(t)}\vec{q}\cdot\vec{n}dS + \int_{\Omega(t)}HdV.\end{aligned} \tag{2.28}$$

Now, if Reynolds transport theorem (2.12) is used on $\int_{\Omega(t)\setminus\Sigma(t)}\frac{1}{2}\rho\frac{D}{Dt}(\vec{v}\cdot\vec{v})dV$, Gauss theorem (2.11) is applied to $\int_{\Gamma(t)}\vec{q}\cdot\vec{n}dS$, and (2.17) to $\frac{D}{Dt}\int_{\Omega(t)}\rho e dV$, we

get locally holding

$$\rho\frac{De}{Dt} = -\nabla\cdot\vec{q} + \boldsymbol{\tau} : \nabla\vec{v} + H \text{ in } \Omega(t)\setminus\Sigma(t), \tag{2.29}$$

$$[\![\vec{q}]\!]\cdot\vec{n} = [\![\vec{v}\cdot\boldsymbol{\tau}]\!]\cdot\vec{n} - [\![(\rho e + \frac{1}{2}\rho\vec{v}\cdot\vec{v})(\vec{v}-\vec{w})]\!]\cdot\vec{n} \text{ in } \Sigma(t). \tag{2.30}$$

Next, the aim is to obtain the heat equation in the form (2.9) as used in several benchmarks in this thesis. Thus we assume the rheological relationship for a classical viscous heat-conducting fluid as follows

$$\tau = -p\mathbb{I} + \boldsymbol{\sigma}(\vec{v}), \lim_{\vec{v}\to 0}\boldsymbol{\sigma}(\vec{v}) = 0, \tag{2.31}$$

where p is the thermodynamic pressure. Further, we employ the relationship known as Fourier law of heat conduction for the heat flow $\vec{q}$

$$\vec{q} = -k\nabla T, \tag{2.32}$$

where k is the thermal conductivity. Now, we utilize the Gibbs relation

$$\rho T\frac{Ds}{Dt} = \rho\frac{De}{Dt} + p\nabla\cdot\vec{v}, \tag{2.33}$$

where s is the entropy per unit mass. By substituting the Eqs. (2.31),(2.32),(2.33) in the local principle for balance of energy (2.29) and (2.30), we obtain

$$\rho T\frac{Ds}{Dt} = -\nabla\cdot(k\cdot\nabla T) + \boldsymbol{\tau} : \nabla\vec{v} + H \text{ in } \Omega(t)\setminus\Sigma(t), \tag{2.34}$$

$$[\![k\nabla T]\!]\cdot\vec{n} = -[\![\vec{v}\cdot\boldsymbol{\tau}]\!]\cdot\vec{n} + [\![(\rho e + \frac{1}{2}\rho\vec{v}\cdot\vec{v})(\vec{v}-\vec{w})]\!]\cdot\vec{n} \text{ in } \Sigma(t). \tag{2.35}$$

The thesis skips the transition from the balance of energy to the heat equation as it requires introducing the whole thermodynamical framework and thus the reader is encouraged to go for more detail into the literature. The derivation is done e.g. in Matyska [2005] and leads to the heat equation in the following form (assuming the dominance of the hydrostatic pressure)

$$\rho c_p\frac{\partial T}{\partial t} = \nabla\cdot(k\nabla T) - \rho c_p\vec{v}\cdot\nabla T - \rho v_r\alpha T g + \boldsymbol{\sigma} : \nabla\vec{v} + H \text{ in } \Omega(t)\setminus\Sigma(t), \tag{2.36}$$

where c_p is the isobaric specific heat, α is the thermal expansion coefficient, v_r is the radial component of velocity and g is now defined as the magnitude of the gravity acceleration $g = |\vec{g}|$ including the acceleration corresponding to the centrifugal forces. In order to get the balance equations in the form of governing equations, several assumptions have to be made which is discussed in the next subsection.

2.2.2 Boussinesq approximation

This subsection continues following Matyska [2005], who presents a derivation of the governing equations for thermal convection in the form that is used in case

of the governing equations (2.1) and (2.2), and the heat transfer equation (2.9) which is a governing equation for some of the benchmarks in the thesis.

This subsection reformulates the fundamental laws of conservation and applies Boussinesq approximation that linearizes the laws of conservation near the reference hydrostatic state $\vec{v} = 0$. The reference pressure p_0, reference density ρ_0, and reference gravity acceleration $\vec{g_0}$ are linked via the local form of the balance of momentum (2.20) assuming $\vec{v} = 0$ and utilizing the rheological relationship (2.31)

$$\nabla p_0 = \rho_0 \vec{g_0} - \rho_0 \vec{\omega} \times (\vec{\omega} \times \vec{x}). \tag{2.37}$$

If we linearize the state equation, which is usually in the form

$$\rho = \rho(p, T), \tag{2.38}$$

and neglect density changes dependent on the dynamic pressure (i.e. deviations from the reference hydrostatic state) $\pi = p - p_0$, we obtain

$$\rho = \rho_0(1 - \alpha(T - T_0)). \tag{2.39}$$

This approximation hides the influence of hydrostatic pressure p_0 and the reference temperature T_0 into a spatial dependence of ρ_0 which is assumed constant in time.

For the continuity equation (2.15), we neglect the thermal expansion (the dependence of ρ on $T - T_0$ in (2.39)) as a part of Boussinesq approximation and obtain the continuity equation

$$\nabla \cdot (\rho_0 \vec{v}) = 0. \tag{2.40}$$

Similarly, the balance of linear momentum (2.20) gets the following form after we use the Eqs. (2.37), (2.39) and the rheological relationship (2.31)

$$\begin{aligned} \rho \frac{D\vec{v}}{Dt} = &-\nabla \pi + \nabla \cdot \boldsymbol{\sigma} + \rho_0 \alpha (T - T_0) \vec{\omega} \times (\vec{\omega} \times \vec{x}) \\ &- 2\rho \vec{\omega} \times \vec{v} + \rho_0 (\vec{g} - \vec{g_0}) - \rho_0 \alpha (T - T_0)(\vec{g} - \vec{g_0}) - \rho_0 \alpha (T - T_0) \vec{g_0}. \end{aligned} \tag{2.41}$$

If we omit the quadratic term $\rho_0 \alpha (T - T_0)(\vec{g} - \vec{g_0})$, the Coriolis force and the thermal expansion on the left-hand side, we get

$$-\nabla \pi + \nabla \cdot \boldsymbol{\sigma} - \rho_0 \alpha (T - T_0) \vec{g_0} + \rho_0 (\vec{g} - \vec{g_0}) = \rho_0 \frac{D\vec{v}}{Dt}. \tag{2.42}$$

The heat equation is linearized by assuming the density independent on the thermal expansion, thus obtaining

$$\rho_0 c_p \frac{\partial T}{\partial t} = \nabla \cdot (k \nabla T) - \rho_0 c_p \vec{v} \cdot \nabla T - \rho_0 v_r \alpha T \vec{g_0} + \boldsymbol{\sigma} : \nabla \vec{v} + Q, \tag{2.43}$$

where Q are heat sources (including internal heating and the heat caused by a decay of radioactive isotopes). This completes the set of Eqs. (2.40),(2.42), and (2.43) that are called the compressible extended Boussinesq approximation of the balance laws of conservation.

Moreover, if we assume the incompressibility, Eq. (2.40) reduces to

$$\nabla \cdot \vec{v} = 0. \tag{2.44}$$

Further, if we assume the fluid is Newtonian,

$$\boldsymbol{\sigma} = 2\eta\dot{\boldsymbol{\epsilon}} = \eta(\nabla\vec{v} + (\nabla\vec{v})^T), \tag{2.45}$$

where η is a constant dynamic viscosity and $\boldsymbol{\epsilon}$ is the strain rate. Next, if we omit the self-gravitation term $\rho_0(\vec{g} - \vec{g_0})$ in (2.42), which is generally about one order lower than the buoyancy term $\rho_0\alpha(T - T_0)\vec{g_0}$, then (2.42) reduces to

$$\rho_0\frac{D\vec{v}}{Dt} = -\nabla\pi + \eta\nabla^2\vec{v} - \rho_0\alpha(T - T_0)\vec{g_0}. \tag{2.46}$$

Finally, we neglect the dissipation $\boldsymbol{\sigma} : \nabla\vec{v}$ and adiabatic heating term $\rho_0 v_r \alpha T g_0$ in the heat equation, assume ρ_0, $\vec{g_0}$, α, c_p and k constant, and suppose Q is spatially constant. Then we obtain the following equation

$$\frac{\partial T}{\partial t} + \vec{v}\cdot\nabla T = \nabla\cdot(\kappa\nabla T) + \frac{Q}{\rho_0 c_p}, \tag{2.47}$$

where $\kappa = \frac{k}{c_p\rho_0}$ is the thermal diffusivity. This completes the set of Eqs. (2.44), (2.46), and (2.47) that are called the classical Boussinesq approximation of the balance laws of conservation.

2.2.3 Nondimensionalisation

The Boussinesq approximation presented in the previous subsection is rescaled in this subsection to nondimensional units. This transformation means, the system of equations does not depend on the particular scale of the quantities, it is rather characterized by dimensionless numbers which characterize the whole system, e.g. Rayleigh, Prandtl, or Reynolds number.

It is useful to define transformation rules between the dimensional and nondimensional form for the basic quantities. Mostly, the favourable choice is to choose some of the SI base units. We follow Matyska [2005] and choose the following transformation rules

$$\vec{x} = \vec{x'}D, t = t'\frac{D^2}{\kappa}, \vec{v} = \vec{v'}\frac{\kappa}{D}, p = \rho_0 g_0 D p', \pi = \frac{\eta_0\kappa}{D^2}\pi', T = T_t + T', Q = \frac{\kappa\Delta T}{D^2}, \tag{2.48}$$

where all quantities with prime symbol are dimensionless, $\vec{x}$ is the position vector, D is the characteristic dimension of the system, η_0 is the reference viscosity, g_0 is the magnitude of $\vec{g_0}$, $\vec{e_z}$ is a unit vector in the vertical direction, and $\Delta T = T_t - T_b$ is the temperature contrast across the layer with T_t at the top and T_b at the bottom. Note, that the pressure p is scaled differently than the dynamic pressure π.

The nondimensionalisation of the classical Boussinesq approximation equations (2.44),(2.46), and (2.47) is done for continuity trivially as follows

$$\nabla' \cdot \vec{v'} = 0. \tag{2.49}$$

For the balance of linear momentum, it is a bit trickier

$$\frac{\rho_0\kappa^2}{D^3}\frac{D\vec{v}}{Dt} = -\frac{\eta_0\kappa}{D^3}\nabla'\pi' + \frac{\eta_0\kappa}{D^3}\eta'\nabla'^2\vec{v}' - \rho_0\alpha\Delta\vec{g_0}T(T' - T_0')\vec{e_z}. \tag{2.50}$$

If the equation is multiplied by $\frac{D^3}{\eta_0\kappa}$, we obtain

$$\frac{1}{Pr}\frac{D\vec{v}}{Dt} = -\nabla'\pi' + \eta'\nabla'^2\vec{v}' - Ra(T' - T_0')\vec{e_z}, \tag{2.51}$$

where the dimensionless number $Pr = \frac{\eta_0}{\rho_0\kappa}$ is the Prandtl number that describes the ratio of momentum diffusivity to thermal diffusivity and $Ra = \frac{\rho_0\alpha g_0\Delta T D^3}{\eta_0\kappa}$ is the Rayleigh number that describes the ratio of time scales for thermal transport via diffusion to thermal transport via convection. For the heat equation, the nondimensionalisation is straightforward

$$\frac{\partial T'}{\partial t'} + \vec{v}'\cdot\nabla'T' = \nabla'^2T + Q'. \tag{2.52}$$

It remains to demonstrate, the Prandtl number is very big and therefore the inertia forces (the left-hand side of the balance of linear momentum equation (2.51)) can be neglected. If we take the values of the setup from thermal convection benchmark by Blankenbach et al. [1989] (specifically case 1a), the values obtained are $Pr = 2.5 \times 10^{25}$, $Ra = 10^4$ which makes the approximation clear. The other benchmarks run in this thesis fulfill this condition as well. The external sources of heat Q are not assumed in any of the benchmarks in the thesis, thus the final set of nondimensional equations is

$$\nabla'\cdot\vec{v}' = 0, \tag{2.53}$$

$$\eta'\nabla'^2\vec{v}' - \nabla'\pi' + Ra(T' - T_0')\vec{e_z} = \vec{0}, \tag{2.54}$$

$$\frac{\partial T'}{\partial t'} + \vec{v}'\cdot\nabla'T' = \nabla'^2T. \tag{2.55}$$

This set of equations is used in the benchmarks in this thesis in section 3.1 and 3.3. It might be modified for the benchmarks with the free surface which corresponds to the section 3.2. The hydrostatic pressure, which is the reference pressure p_0, cannot be subtracted due to the stability of the numerical solution. In this case, we can use $\nabla\pi = \nabla p - \rho_0 g_0$ instead, where the centrifugal term from (2.37) is neglected. Moreover, different scaling is used for p than for π, and hence we get the equation (2.54) in the following form

$$\eta'\nabla'^2\vec{v}' - \frac{Ra}{\alpha\Delta T}\nabla'p' + Ra(T' - T_0')\vec{e_z} - \frac{Ra}{\alpha\Delta T}\vec{e_z} = \vec{0}. \tag{2.56}$$

2.2.4 Viscoplastic rheology and strain weakening

The benchmark in section 3.4 and the final application to Europa in section 4.1 follow a non-linear viscoplastic rheology in order to describe a response of the crustal material to stress. The thesis follows the description and setup done by

Maierová [2012] in order to benchmark the viscoplastic deformation and strain weakening to previously existing results.

The plasticity is an approximate way of modelling brittle failure that is present at low temperature and high strain rates. This is the case for the chaotic terrains in the formation process. Both the plastic and viscous deformation are irreversible, however, the plastic deformation occurs only if the overall stress reaches a point called yield stress σ_Y whereas the viscous deformation is always present in the model in this thesis.

The rheological relationship follows

$$\boldsymbol{\sigma} = 2\eta_{eff}\dot{\boldsymbol{\epsilon}}, \tag{2.57}$$

where η_{eff} is comprised of its viscous η_v and plastic part η_p as in Eq. (2.6 where the latter might be defined from the relation that holds in the plastic regime

$$\eta_p = \frac{\sigma_Y}{2\dot{\boldsymbol{\epsilon}}^{II}}, \tag{2.58}$$

where $\dot{\boldsymbol{\epsilon}} = \frac{1}{2}(\nabla\vec{v} + (\nabla\vec{v})^T)$ is the strain rate. The yield stress σ_Y is, however, not independent and can be chosen based on empirical research which is summarized e.g. in Ranalli [1995]. The yield criterion used in this thesis follows the choice from Maierová [2012] who chose Drucker-Prager criterion used in Earth's applications for the modelling of the rock behaviour, in the following form

$$\sigma_Y = p\sin\phi + C\cos\phi, \tag{2.59}$$

where p is the pressure, C is the Cohesion, ϕ is the angle of internal friction. The derivation of the Drucker-Prager criterion can be done from the Mohr-Coulomb criterion which describes the given plane where the material yields from the perspective of normal stress σ_n and shear stress σ_t by the following relationship

$$\sigma_t = \sigma_n \tan\phi + C. \tag{2.60}$$

The detailed derivation of Eq. (2.59) from the Mohr-Coulomb criterion (2.60) can be found in Maierová [2012].

In case of dry rocks, the angle of internal friction ϕ is around 30°[Maierová, 2012], which is also the choice for the final application to Europa in this thesis. The benchmark in chapter 3.4 is run for the angles 10°, 20°, and 30°.

There is a numerical issue regarding the singular value of σ_Y in case of $\sigma_n \leq 0$ which is treated in the literature modelling the shear bands in geodynamic numerical simulations (e.g. [Lemiale et al., 2008], [Kaus, 2010]) by adding the cutoff term σ_{min} which ensures the yield stress σ_Y cannot fall below the value

$$\sigma_Y = \max(\sigma_{min}, p\sin\phi + C\cos\phi). \tag{2.61}$$

This mode does not fully correspond to the experimentally observed relationship, which exhibits steeper slope in the domain where $\sigma_n < 0$, and more flattened slope otherwise [Ranalli, 1995]. Moreover, the stress at yield seems to behave more complexly which is different depending on whether the friction starts from static or dynamic state. [Maierová, 2012]

A solution to handle these inconsistencies at long time scales lies in adding an important mechanism observed experimentally by Bos and Spiers [2002] called

strain weakening. This phenomenon proved reasonable for the crustal deformation at long time scales and it is specified by a decrease of friction at regions where the local accumulation of strain caused change in the material characteristics. The approximation of the strain weakening process can be done by assuming the cohesion (or angle of internal friction) decreasing linearly with the plastic part of the strain and having cutoff values C_0 and C_∞ with $C_0 > C_\infty$ as was done e.g. in [Gerya, 2010]

$$C = \begin{cases} C_0 & \text{if } \boldsymbol{\epsilon}_p^{II} \leq \epsilon_0 \\ C_0 + (C_\infty - C_0)\left(\frac{\boldsymbol{\epsilon}_p^{II} - \epsilon_0}{\epsilon_\infty - \epsilon_0}\right) & \text{if } \epsilon_0 < \boldsymbol{\epsilon}_p^{II} < \epsilon_\infty \\ C_\infty & \text{if } \boldsymbol{\epsilon}_p^{II} \geq \epsilon_\infty. \end{cases} \tag{2.62}$$

The final setup (application to Europa in section 4.1) assumes that the effective viscosity is comprised of both plastic and viscous part as was stated in Eq. (2.6). This requires solving the advection equation (2.3) for plastic strain $\boldsymbol{\epsilon}_p$ as the strain weakening occurs due to the plastic part of the strain, which is why the thesis specifies in Eq. (2.62) that the plastic part of the strain is used.

2.2.5 Weak formulation

The weak formulation of the governing equations is defined assuming the test functions from the following functional spaces as in Taylor and Hood [1973], ensuring the existence of derivatives and the possibility of setting up Taylor-Hood finite elements triangulation

$$V := \{\vec{v} \in C(\Omega^d) | \vec{v} \text{ is a piecewise quadratic function in } \Omega\}, \tag{2.63}$$

$$P := \{p \in C(\Omega) | \text{p is a piecewise linear function in } \Omega\}, \tag{2.64}$$

$$T := \{t \in C(\Omega) | \text{t is a piecewise quadratic function in } \Omega\} \tag{2.65}$$

where d is the number of spatial dimensions.

The test function testing for the pressure field is denoted $\xi \in P$, the test function testing for the velocity is denoted $\vec{\psi} \in V$ where these two spaces are forming a mixed element space in the finite element numerical implementation. The test function for the temperature in the heat equation is denoted $\varphi \in T$.

The weak formulation of the continuity equation is obtained simply by taking the integral over the domain

$$\int_\Omega (\nabla \cdot \vec{v}) \xi dV = 0. \tag{2.66}$$

The balance of momentum equation is obtained similarly by using integration by parts method

$$\int_\Omega (-\nabla p + \nabla \cdot \sigma + Ra(T - T_0)\vec{e}_z)\vec{\psi} dV = \vec{0}, \tag{2.67}$$

$$-\int_\Omega \sigma : \nabla\vec{\psi} dV + \int_{\partial\Omega} \underbrace{\sigma\vec{\psi}\cdot\vec{n}}_{=0} dS + \int_\Omega Ra(T-T_0)\vec{e}_z\vec{\psi}dV = 0, \tag{2.68}$$

obtaining the final result

$$\int_\Omega p(\nabla\cdot\vec{\psi})dV - \int_\Omega \sigma : \nabla\vec{\psi}dV + \int_\Omega Ra(T-T_0)\vec{e}_z\vec{\psi}dV = 0. \tag{2.69}$$

The weak formulation for heat equation is obtained in the same way as the balance of momentum equation utilizing the integration by parts method

$$\int_\Omega \frac{\partial T}{\partial t}\varphi + \vec{v}\cdot\nabla T\varphi dV = \int_\Omega \Delta T\varphi dV, \tag{2.70}$$

$$\int_\Omega \frac{\partial T}{\partial t}\varphi + \vec{v}\cdot\nabla T\varphi dV = \int_{\partial\Omega} \underbrace{\vec{n}\cdot\nabla T}_{=0}\varphi - \int_\Omega \nabla T\cdot\nabla\varphi dV, \tag{2.71}$$

resulting in the final form

$$\int_\Omega \frac{\partial T}{\partial t}\varphi + \vec{v}\cdot\nabla T\varphi dV = -\int_\Omega \nabla T\cdot\nabla\varphi dV. \tag{2.72}$$

2.3 Arbitrary Lagrangian Eulerian Method

2.3.1 Motivation

This subsection aims to motivate the use of the Arbitrary Lagrangian Eulerian (ALE) method. In mathematical models used in continuum mechanics, the problem is usually described either in referential or in actual configuration. The former is called the Lagrangian specification or Lagrangian frame of reference and the flow field is observed by following an individual parcel moving through space and time. The latter is called the Eulerian specification or the Eulerian frame of reference and the flow field is observed in a fixed location where the material flows as the time passes.

The Lagrangian frame of reference is often preferred in the mechanical applications where the initial state of the domain Ω_X is clearly defined. Hence, if the deformations are not too distortive, the system is able to track each parcel individually and the simulation is well specified. On the other hand, if the deformations are not negligible, the mesh might be completely disrupted. That might lead to connecting points related to the underlying mesh which are distant from each other and would not only make the numerical simulation very unstable, but the resulting quantities might also suffer from badly defined derivatives or other model misspecification.

The Eulerian frame of reference comes as a useful tool in cases where the Lagrangian referential frame cannot be easily used, e.g. in case of fluids where the distortions are generally significant but the exact location of the specific particles or the position of some structure interface is not important for the problem. The domain in the Eulerian reference frame is denoted Ω_x and the relation between the Lagrangian and Eulerian reference frame is given by the mapping $\vec{\chi}$ defined as

$$\vec{\chi} : \Omega_X \times I \to \Omega_x \times I; \chi(\vec{X}, t) \mapsto (\vec{x}, t), \tag{2.73}$$

where $I = [t_0; t_{end}]$ is the time interval of the process, $X \in \Omega_X$, $x \in \Omega_x$, and $t \in I$.

The generalization of both referential frames is the ALE method which can find its applications especially in the problems where there is an interaction between the internal fluid flow and some moving structure. These fluid-structure interaction problems are frequently studied in engineering systems such as aircraft, spacecraft and bridges design. The analytical mathematical approach is often too complex for these problems and therefore the experiments or numerical simulations are often preferred. [Sigrist, 2015]

The ALE method is a practical method how to deal with problems defined by finite elements method where the domain of interest is either moving or coping with strong distortions while allowing for a clear way how to treat free surfaces and fluid-fluid or fluid-structure interfaces. [Donea et al., 1982] The deformation of the domain is changing the way how to treat the quantities at the specific mesh nodes. The aim of the method is to make the movement of the underlying mesh possible and to not change the form of the equations used to solve the problem significantly. The exact mechanism how to do that is explained in the following subsection.

2.3.2 Kinematics

This subsection provides a mathematical framework to deal with the mesh movement in the solved problem. The geometry of the problem is specified by the Fig. 2.3 where the Ω_X denotes the Lagrangian reference frame, Ω_x denotes the Eulerian reference frame, and Ω denotes the Arbitrary Lagrangian Eulerian reference frame, which basically corresponds to the referential frame of the undeformed mesh.

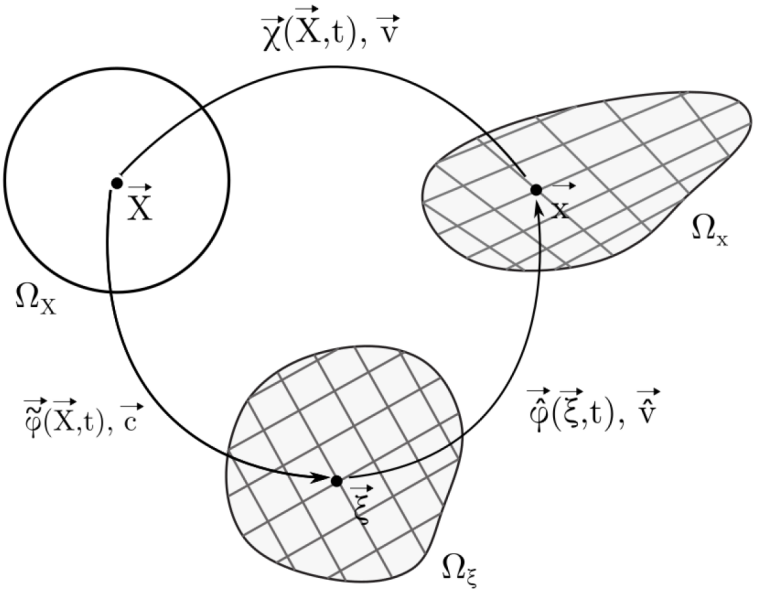

Figure 2.3: Schema depicting the relationship between the ALE configuration, the actual configuration and the reference configuration

The mappings between the respective referential frames are depicted in the figure but only the $\vec{\chi}$ mapping was defined in the Eq. (2.73). The mapping

between the Lagrangian reference frame and the ALE reference frame is denoted by $\vec{\tilde{\varphi}}$ and is defined in the following way

$$\vec{\tilde{\varphi}} : \Omega_X \times I \to \Omega_\xi \times I; \tilde{\varphi}(\vec{X}, t) \mapsto (\vec{\xi}, t). \tag{2.74}$$

Similarly, the mapping between the ALE reference frame and the Eulerian reference frame is defined as

$$\vec{\hat{\varphi}} : \Omega_\xi \times I \to \Omega_x \times I; \hat{\varphi}(\vec{\xi}, t) \mapsto (\vec{x}, t). \tag{2.75}$$

The interpretation of these mappings is very intuitive if understood as in the Fig. 2.3. The mapping $\vec{\tilde{\varphi}}$ assigns the point from the Lagrangian reference state a point in the mesh (ALE reference frame) whereas the mapping $\vec{\hat{\varphi}}$ assigns the actual Eulerian configuration for the each point of the mesh. This mathematical framework enables us to move the mesh in the computations and is used in all computations throughout the thesis where the free surface boundary condition is assumed.

The material velocity implicitly resulting from the mapping between the Lagrangian and Eulerian reference frame is given by the following relationship

$$\vec{v}(\vec{x}, t) = \left.\frac{\partial \vec{\chi}}{\partial t}\right|_{\vec{X}}. \tag{2.76}$$

The deformation gradient is defined in a standard continuum-mechanics way as

$$\mathbb{F} = \nabla_X \vec{\chi}, \tag{2.77}$$

where ∇_X denotes the derivative with respect to the spatial coordinates in the Lagrangian reference frame. The material time derivative of an arbitrary scalar value in the Eulerian reference frame can be defined as

$$\dot{\alpha} = \left.\frac{\partial \alpha}{\partial t}\right|_{\vec{X}}, \tag{2.78}$$

which is rewritten as

$$\dot{\overline{\alpha(x,t)}} = \dot{\overline{\alpha(\vec{\chi}(\vec{X}, t), t)}} = \left.\frac{\partial \alpha}{\partial t}\right|_{\vec{x}} + \vec{v} \cdot \nabla_x \alpha. \tag{2.79}$$

The mapping between the ALE configuration and the Eulerian reference frame $\hat{\varphi}$ defines the displacement as

$$\vec{\hat{u}} = \vec{\hat{\varphi}}(\vec{\xi}, t) - \vec{\hat{\varphi}}(\vec{\xi}, 0), \tag{2.80}$$

and velocity as

$$\vec{\hat{v}} = \left.\frac{\partial \hat{\varphi}}{\partial t}\right|_{\vec{\xi}} = \left.\frac{\partial \hat{u}}{\partial t}\right|_{\vec{\xi}}. \tag{2.81}$$

2.3.3 Free surface implementation

In order to model the mesh movement resulting from the free surface deformation, the kinematic framework for ALE method from the previous section 2.3.2 will be used. The mesh nodes $\vec{\xi} = (\xi_x, \xi_z)$ corresponding to the top boundary are the points in the actual configuration $\vec{x} = (x, z)$ in each time t, hence

$$x(t) = \xi_x, z(t) = \hat{\varphi}(\xi_x, \xi_z, t) = \hat{\varphi}(x, \xi_z, t) \text{ on } \Gamma_T. \tag{2.82}$$

We can define a function $h(x,t) := \hat{\varphi}(x, \xi_z, t)|_{\vec{\xi} \in \Gamma_T}$ which returns a z component of $\vec{x}$ corresponding to the top boundary for a given component x and time t.

This approach enables us to assume the mesh displacement in the horizontal direction to be zero at boundaries $\Gamma_R \cup \Gamma_L$ as the free surface is only at the top boundary Γ_T. Therefore, the quantity h also changes only with the vertical movement of the mesh. This gives us a kinematic relationship for the top boundary

$$z(t) = h(x,t) \text{ on } \Gamma_T. \tag{2.83}$$

Let us take a derivative of this equation to obtain

$$\frac{\partial h}{\partial x} v_x + \frac{\partial h}{\partial t} = v_z, \text{ on } \Gamma_T, \tag{2.84}$$

where $\vec{v} = (v_x, v_z)$ in the actual configuration. This gives us a framework to estimate the mesh displacement at the top boundary Γ_T, however, it is necessary to harmonically extend h so we have the definition of $\hat{\varphi}$ in the whole domain Ω so that

$$\hat{\varphi}|_{\Gamma_T} = h. \tag{2.85}$$

The solution to adaptively distribute the mesh points as a response to the free surface deformation is to assume that the mesh node location $\hat{\varphi}(\vec{\xi}, t)$ is governed by the Poisson equation in Ω

$$\nabla^2 \hat{\varphi} = 0. \text{ in } \Omega, \tag{2.86}$$

with the boundary conditions

$$\frac{\partial \hat{\varphi}}{\partial \hat{\varphi}} v_x + \frac{\partial h}{\partial t} = v_z, \text{ on } \Gamma_T, \tag{2.87}$$

$$\frac{\partial \hat{\varphi}}{\partial x} = 0 \text{ on } \Gamma_T, \tag{2.88}$$

$$\hat{\varphi} = 0 \text{ on } \Gamma_B, \tag{2.89}$$

which means the boundary conditions for this problem are assumed in the form of zero value at the bottom boundary and assumes mesh cannot move through the side boundaries. The other possibility is to assume the horizontal component fixed, which is reasonable if the vertical movements dominate and the horizontal component is stable. In such a case we have

$$\frac{\partial \hat{\varphi}}{\partial x} = 0 \text{ in } \Omega, \tag{2.90}$$

which reduces the problem 2.86 to

$$\frac{\partial^2 \hat{\varphi}}{\partial z^2} = 0 \text{ in } \Omega, \tag{2.91}$$

assuming the horizontal movement of the mesh fixed. In both choices of boundary conditions, the evolution of the mesh is numerically obtained in $k+1$-th step from the following equation given value of mesh deformation $\hat{\varphi}$ in k-th step $\hat{\varphi}^k$

$$\frac{\hat{\varphi}^{k+1} - \hat{\varphi}^k}{\Delta t} + v_x \frac{\partial \hat{\varphi}^{k+1}}{\partial x} - v_z = 0. \tag{2.92}$$

The numerical implementation of the free surface in this thesis suffers also from the negligence of the inertial term which may cause that the numerical implementation is not sensitive to large scale changes in the magnitude of velocity. This might cause numerical instability gradually increasing the amplitude of the oscillations of the free surface. This phenomenon was addressed by Kaus et al. [2010] who provide a solution to this problem. The key is to add a corrective term adding a force to the balance of linear momentum equation in the following form $\lambda \rho \vec{f}(\vec{v} \cdot \vec{n}) \Delta t$ on Γ_T where $\vec{f}$ is the force assumed in our model as $\vec{f} = \frac{Ra}{\alpha \Delta T}(1 - \alpha \Delta T T)\vec{e_z}$, and λ is a sensitivity parameter, assumed $\lambda = 1.0$.

2.3.4 Nitche's method for general boundary conditions

This subsection follows the paper by Juntunen and Stenberg [2009] who provide a framework for treating general boundary conditions in the finite element method extending the original Nitsche's method. The paper shows how to generalize the boundary condition specification for problems where Dirichlet boundary condition might not be easily numerically handled. This is the case for the free surface boundary used in several benchmarks in the thesis where we suppose the existence of free surface. The paper shows that the Nitsche's method can be generalized on the whole class of problems by showing the derivation for the Poisson problem. Let us suppose the function of interest is u given the righ hand side f as in Juntunen and Stenberg [2009].

$$-\Delta u = f \text{ in } \Omega, \tag{2.93}$$

$$u = u_0 \text{ on } \Gamma \tag{2.94}$$

,

where u_0 is a prescribed boundary value. The following approximation (called Ritz approximation) replaces the Dirichlet boundary condition by the Neumann condition

$$\frac{\partial u}{\partial n} = \frac{1}{\epsilon}(u_0 - u) + g \text{ on } \Gamma, \tag{2.95}$$

where $\epsilon > 0$ is a small parameter, and n is a normal. Such an approximation leads to the convergence of the new boundary condition 2.95 to the Dirichlet problem 2.94 as the ϵ approaches zero. The problem of this approach is that the finite element discretization is getting ill-conditioned, and hence there is a need to show the method can use the Neumann condition to substitute the Dirichlet condition in case of free surface. [Juntunen and Stenberg, 2009]

The authors of the article present the following equations as the Nitsche's method.

$$\mathcal{B}_h(u_h, v) = \mathcal{F}_h(v) \forall v \in V_h \tag{2.96}$$

where V_h is defined in the paper as a space of piecewise polynomial function of degree p. The forms are defined by

$$\begin{aligned}\mathcal{B}_h(u,v) =&(\nabla u, \nabla v)_\Omega + \sum_{E\in\mathcal{G}_h} -\frac{\gamma h_E}{\epsilon+\gamma h_E}\left[\langle\frac{\partial u}{\partial n}, v\rangle_E + \langle u, \frac{\partial v}{\partial n}\rangle_E\right] \\ &+\frac{1}{\epsilon+\gamma h_E}\langle u, v\rangle_E - \frac{\epsilon\gamma h_E}{\epsilon+\gamma h_E}\langle\frac{\partial u}{\partial n}, \frac{\partial v}{\partial n}\rangle_E\end{aligned} \tag{2.97}$$

$$\begin{aligned}\mathcal{F}_h(v) = (f,v)_\Omega + &\sum_{E\in\mathcal{G}_h}\frac{1}{\epsilon+\gamma h_E}\langle u_0, v\rangle_E - \frac{\gamma h_E}{\epsilon+\gamma h_E}\langle u_0, \frac{\partial v}{\partial n}\rangle_E \\ &+\frac{\epsilon}{\epsilon+\gamma h_E}\langle g, v\rangle_E - \frac{\epsilon\gamma h_E}{\epsilon+\gamma h_E}\langle g, \frac{\partial v}{\partial n}\rangle_E\end{aligned} \tag{2.98}$$

where γ is a bounded positive parameter and $h := \max\{h_K : K \in \mathcal{T}_h\}$ where $\mathcal{T}_h$ is a triangulation of Ω. By taking the limit $\epsilon \to 0$, the resulting equation for the Poisson equation is the following

$$\int_\Omega \nabla u \cdot \nabla v dx = \sum_{E\in\mathcal{G}_h}\int_E (u_0 - u)\left(\frac{1}{\gamma h_E}v - \frac{\partial v}{\partial n}\right) + \frac{\partial u}{\partial n} dS. \forall v \in V_h \tag{2.99}$$

This equation can be used in the free surface application in the thesis if $u = \hat{\varphi}$ as the term $u_0 - u$ in Eq. (2.100) can be substituted now with the equation (2.92) (we change the notation of the test function v to w in order to not confuse the reader as the Eq. (2.92) works with the velocity components v_x and v_z)

$$\begin{aligned}&\int_\Omega \nabla\hat{\varphi}^{k+1}\cdot\nabla w dx = \\ &= \sum_{E\in\mathcal{G}_h}\int_E(\hat{\varphi}^{k+1} - \hat{\varphi}^k + \Delta t v_x\frac{\partial\hat{\varphi}^{k+1}}{\partial x} - \Delta t v_z)\left(\frac{1}{\gamma h_E}w - \frac{\partial w}{\partial n}\right) + \frac{\partial\hat{\varphi}^{k+1}}{\partial n}dS. \forall w \in V_h.\end{aligned} \tag{2.100}$$

This presents a way how to formulate the boundary conditions in a weak form for the mesh displacement without the need to impose a Dirichlet condition (for more details, see Juntunen and Stenberg [2009]).

2.4 Numerical methods

This chapter aims to explain the numerical methods used in the benchmarks and the final application to Europa.

2.4.1 Crank-Nicolson scheme

A better stability of the numerical solution of heat equation in the thermal convection benchmarks can be handled by assuming either semi-implicit or fully

implicit numerical scheme in which we follow Crank and Nicolson [1947]. We assume the general parameter $\theta \in [0, 1]$ changes whether the schema is semi implicit ($\theta = 0.5$) or implicit ($\theta = 1$) or other choice. This means to discretize the equation (2.9) as

$$\frac{T^{k+1} - T^k}{\Delta t} + \theta(\vec{v} \cdot \nabla T^{k+1} - \nabla^2 T^{k+1}) + (1 - \theta)(\vec{v} \cdot \nabla T^k - \nabla^2 T^k) = 0 \quad (2.101)$$

where Δt is the time step in the discrete problem. This numerical scheme is used in benchmarks in sections 3.1, 3.2, 3.3 where we assume semi-implicit scheme $\theta = 0.5$.

2.4.2 Taylor-Hood elements

The finite elements in the thesis are chosen in order to guarantee a unique numerical solution of the problem which is a known property resulting from the fact that the Taylor-Hood elements satisfy a discrete inf-sup condition [Arndt, 2013]. The thesis chooses the finite elements introduced by Taylor and Hood [1973] in a form of crossed rectangular Lagrange elements of order P^2 for velocity $\vec{v}$ and P^1 for pressure p in the Stokes problem defined by equations 2.53 and 2.54, or possibly altering the 2.54 for 2.56 in case of free surface. The spaces for the Taylor-Hood elements are defined on a triangulation $\mathcal{T}_h$ of the entire Ω domain. The spaces are defined as follows

$$V_h := \{\vec{v} \in C(\Omega^d); \vec{v}|_K \in \mathcal{P}_2(K)^d \ \forall K \in \mathcal{T}_h\}, \quad (2.102)$$

$$P_h := \{p \in C(\Omega); p|_K \in \mathcal{P}_1(K) \ \forall K \in \mathcal{T}_h\}, \quad (2.103)$$

$$T_h := \{t \in C(\Omega); t|_K \in \mathcal{P}_2(K) \ \forall K \in \mathcal{T}_h\} \quad (2.104)$$

where d is the number of spatial dimensions, and space of temperature functions is assumed comprised of piecewise quadratic polynomials due to the improved accuracy of the solution. The formulation of the discretized problem in a weak form is as follows for the thermal convection setup

$$\sum_{K \in \mathcal{T}_h} \int_K (\nabla \cdot \vec{v}) \xi dV = 0, \quad (2.105)$$

$$\begin{aligned} &\sum_{K \in \mathcal{T}_h} \int_K p(\nabla \cdot \vec{\psi}) dV - \sum_{K \in \mathcal{T}_h} \int_K \sigma : \nabla \vec{\psi} dV \\ &+ \sum_{K \in \mathcal{T}_h} \int_K Ra(T - T_0) \vec{e}_z \vec{\psi} dV = 0, \end{aligned} \quad (2.106)$$

$$\sum_{K \in \mathcal{T}_h} \int_K \frac{\partial T}{\partial t} \varphi + \vec{v} \cdot \nabla T \varphi dV = - \sum_{K \in \mathcal{T}_h} \int_K \nabla T \cdot \nabla \varphi dV. \quad (2.107)$$

2.4.3 Picard iterations

The thesis uses Picard iterations for the handling of the non-linearity in the Stokes equation solving for velocity field. The key idea is that the nonlinear term can be discretized by using of the Picard iterations, which means transform the non-linear problem to a series of linear problems possible to solve by linear solver which converge to the same solution. [Logg et al., 2012] In case of this equation the nonlinear term can be linearized by assuming the following scheme from Segal and Vuik [1995]

$$v^{k+1} \cdot \nabla v^{k+1} \approx v^{k} \cdot \nabla v^{k+1}, \tag{2.108}$$

the alternative approach is to use the Newton scheme

$$v^{k+1} \cdot \nabla v^{k+1} \approx v^{k} \cdot \nabla v^{k+1} + v^{k+1} \cdot \nabla v^{k} - v^{k} \cdot \nabla v^{k}. \tag{2.109}$$

The usual choice in case of non-linearity e.g. in Stokes equation is to proceed with a number of Picard iterations [Segal and Vuik, 1995]. This means to discretize the Eq. 2.2 to the following iterations

$$-\nabla p + \nabla \cdot \eta_{eff}(v^{k})(\nabla \vec{v^{k+1}} + (\nabla \vec{v^{k+1}})^{T}) + \rho_{ice}\vec{g} = \vec{0}, \tag{2.110}$$

which linearize the nonlinearity as the η_{eff} is dependent on the velocity through the dependence on $\dot{\boldsymbol{\epsilon}}$.

2.4.4 Discontinuous Galerkin Elements

In order to model the strain weakening effect in benchmark in 3.4 and final application to Europa 4.1, it is necessary to solve the advection equation for the plastic strain in the following form

$$\frac{\partial \boldsymbol{\epsilon}_{\boldsymbol{p}}^{II}}{\partial t} + \vec{v} \cdot \nabla \boldsymbol{\epsilon}_{\boldsymbol{p}}^{II} = \dot{\boldsymbol{\epsilon}}_{p}^{II}, \tag{2.111}$$

where $\boldsymbol{\epsilon}_{\boldsymbol{p}}^{II}$ is the second invariant of the plastic strain defined as $\sqrt{\frac{1}{2}\boldsymbol{\epsilon}_{\boldsymbol{p}}^{II} : \boldsymbol{\epsilon}_{\boldsymbol{p}}^{II}}$. The motivation for the use of discontinuous Galerkin elements comes from the occurence of very high contrasts in the magnitude of the plastic strain variable in the numerical model corresponding to this equation. The solution is to choose the discontinuous Galerkin elements in a similar framework as presented in Di Pietro et al. [2006] who tackled the problem of the evolution of the interface of two materials. We proceed by multiplying the equation by the test function $\phi_h \in V_h$ where $V_h = \{v_h \in L^2(\Omega) | v_h|_K \in \mathbb{P}_k(K), \forall K \in T_h\}$ and by integrating the whole equation over a sum of elements $K \in T_h$ where T_h is a triangulation of the domain Ω.

$$\sum_{K \in T_h} \int_K \phi_h \frac{\partial \epsilon_{p,h}^{II}}{\partial t} dx + \sum_{K \in T_h} \int_K \phi_h \vec{v} \cdot \nabla \epsilon_{p,h}^{II} dx = 0. \tag{2.112}$$

where $\epsilon_{p,h}^{II}$ is the second invariant od the plastic strain computed on the space of functions V_h restricted to the elements of triangulation.

After an application of Green's formula to the second integral the following integrals can be obtained which can be rewritten in terms of jumps and averages of quantities as follows

$$\begin{aligned} &\sum_{K\in T_h}\int_K \phi_h \frac{\partial \epsilon_{p,h}^{II}}{\partial t} dx - \sum_{K\in T_h}\int_K \epsilon_{p,h}^{II}\vec{v}\cdot\nabla\phi_h dx \\ &+\sum_{e\in E^0}\int_e \vec{v}\cdot[[\phi_h]]\{\epsilon_{p,h}^{II}\} + \frac{1}{2}|\vec{v}\cdot\vec{n}|[[\phi_h]]\cdot\{\epsilon_{p,h}^{II}\}d\sigma \\ &+\sum_{e\in E^\partial}\int_e \mathbf{v}\cdot[[\phi_h]]\{\epsilon_{p,h}^{II\,*}\}d\sigma = 0 \end{aligned} \tag{2.113}$$

where $\{f\} = \frac{1}{2}(f^+ + f^-)$ is the definition of averaging, $[\![f]\!] = f^+\vec{n}^+ + f^-\vec{n}^-)$ is the definition of jump for the scalar quantity f and normal vector $\vec{n}$, the last thing that remains is to define $\epsilon_{p,h}^{II\,*} = \epsilon_{p,h}^{II}$ if $\vec{v}\cdot\vec{n} > 0$ and $\epsilon_{p,h}^{II\,*} = \epsilon_{p,h}^{II}$ if $\vec{v}\cdot\vec{n} \leq 0$ (for more details see Di Pietro et al. [2006]). This is the treatment of the discontinuous $\epsilon_{p,h}^{II}$ in the shear band benchmark and the application to Europa.

3. Benchmarks

In this chapter, the aim is to perform several tests in order to validate the numerical methods used in the final application. The tests are based on numerically tested setups previously evaluated by other researchers. This enables the author to simulate the processes on Europa and to be in line with the numerical implementation of the models previously validated by the geophysics researchers with application to other extraterrestrial bodies.

3.1 Thermal Convection Benchmark

This section is focused on the thermal convection benchmark made by Blankenbach et al. [1989] who compared several computational codes that solve a thermal convection problem in a fixed domain setting. This benchmark has soon become a natural first step in geophysical and geodynamical research communities due to its relatively easy implementation and usefulness in many advanced geodynamical applications. Blankenbach benchmark is a simple tool to correct the numerical computations in early stages as it builds on a well defined setup which can be replicated regardless of the choice of the software for partial differential equations modelling.

3.1.1 Governing equations

The governing equations for the Blankenbach benchmark follow from the Boussinesq approximation which was described in detail in the subsection 2.2.2. In order to introduce the benchmark setup, the basic properties of the approximation will be reminded.

This approximation linearizes the conservation laws near a reference hydrostatic state when $\vec{v} = 0$. The linearization of the state equation is done with respect to the temperature deviations resulting in the form of the density $\rho = \rho_0(1-\alpha(T-T_0))$ where ρ_0 and T_0 are assumed constant in time. The approximation neglects the thermal expansion everywhere except for the term with gravity force and neglects the selfgravity $\rho_0(g - g_0) \to 0$. The benchmark assumes to work with viscous fluid, where the viscosity η might be in general case function of temperature or pressure. After the nondimensionalisation, which was discussed in the subsection 2.2.3, the inertia forces were neglected, and thus the resulting equations were obtained in the following nondimensional form (prime symbols are omitted) following the general result of subsection 2.2.3.

The first equation in the system is the continuity equation

$$\nabla \cdot \vec{v} = 0, \tag{3.1}$$

where $\vec{v}$ is the velocity, This equation is followed by the balance of momentum equation

$$-\nabla\pi + \nabla \cdot \boldsymbol{\sigma} + Ra(T - T_0)\vec{e}_z = \vec{0}, \tag{3.2}$$

where π is the dynamic pressure (which without loss of generality fixed in the

upper left corner of the domain as it is defined up to a constant), Ra is the Rayleigh number, T is the temperature, T_0 is the reference temperature, and $\vec{e}_z$ is the unit vector in the vertical direction. The last equation of this system is the heat equation with no heat sources Q

$$\frac{\partial T}{\partial t} + \vec{v} \cdot \nabla T = \Delta T, \tag{3.3}$$

where t is the time.

3.1.2 Problem geometry

The problem is defined on a rectangular 2D domain Ω with boundary $\Gamma = \partial\Omega$. The bottom boundary Γ_B is continuously heated by a source of energy on a constant temperature T_b whereas the top boundary Γ_T is continuously cooled down to a constant temperature T_t. The difference of the temperature is denoted as $\Delta T = T_b - T_t$.

The side boundaries $\Gamma_L \cup \Gamma_R$ of the domain are assumed to be thermally insulating $\nabla T \cdot \vec{n} = 0$. The contact of the fluid with the boundary is defined by a free slip boundary condition with no inflow and outflow through the boundary $\boldsymbol{\sigma} \cdot \vec{n} = 0$, $\vec{v} \cdot \vec{n} = 0$ which allows the liquid to freely flow without the tension at the boundaries. The whole setup is depicted in the following schema in Fig. 3.1.2

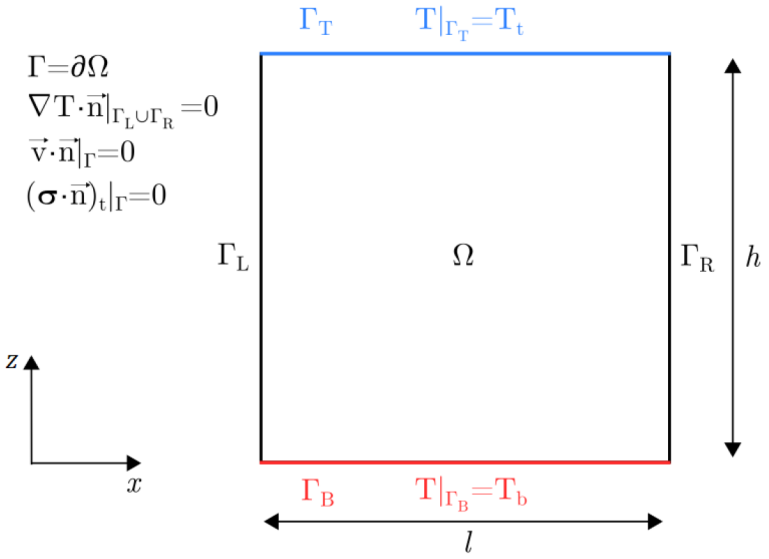

Figure 3.1: The schema of the problem geometry for the thermal convection benchmark

In order to simulate steady state, it is necessary to begin with a non-balanced initial temperature distribution which is in our case modelled by a small sinusoidal deviation from the balanced linearly decreasing temperature field given by the following equation

$$T(x, z) = 1 - z + 0.01 \cos(\pi x) \sin(\pi z), \tag{3.4}$$

where x and z are the spatial coordinates.

3.1.3 Results

In the following Fig. 3.2, there is a time evolution of the temperature field showing the initial temperature distribution (a), the state after five steps of simulation reaching the nondimensional time $t = 0.0075$ (b) and the steady state after many steps reaching the nondimensional time $t = 0.5000$ (c).

Similarly, the Fig. 3.3 is depicting the evolution of the velocity field evaluated by its magnitude again showing the initial state (a), the state after five steps of simulation (b) and the steady state (c).

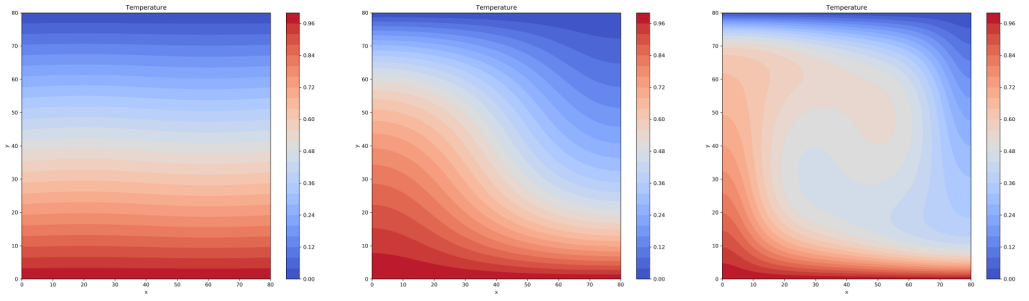

(a) t=0.0000 (b) t=0.0075 (c) t=0.5000

Figure 3.2: Evolution of the temperature field in the thermal convection benchmark

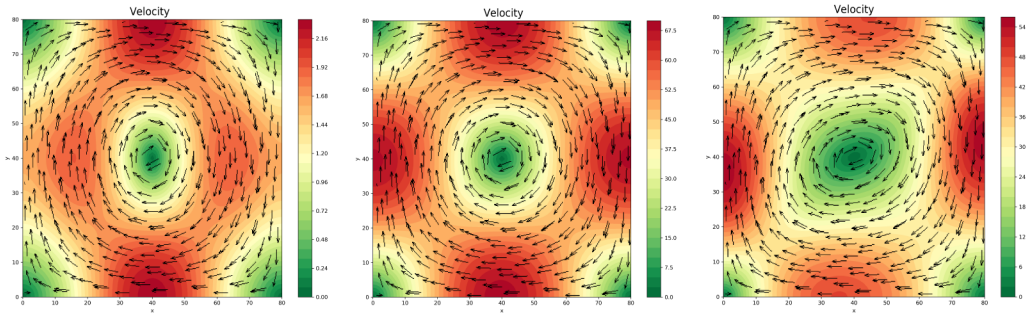

(a) t=0.0000 (b) t=0.0075 (c) t=0.5000

Figure 3.3: Evolution of the velocity field in the thermal convection benchmark

All of the presented results are perfectly in line with the benchmark values which can be evaluated by comparing the time evolution of the several quantities that characterize the field evolution. First of the benchmark values is the Nusselt number defined as

$$Nu = -h \frac{\int_0^l \frac{\partial T}{\partial z}(x)\Big|_{z=h} dx}{\int_0^l T(x)\Big|_{z=0} dx}, \tag{3.5}$$

where h is the height of the domain and l is the width of the domain. The Nusselt number is the ratio of convective to conductive heat transfer at boundaries (here $z = 0$ and $z = h$) and the higher the number is, the more active is the convection.

The Nusselt number evolution is depicted in the Fig. 3.4 a) where it can be seen it converges to the same value both in our simulation and in the benchmark

which confirms the implementation was successful. Second studied quantity is the root mean square velocity defined as

$$v_{rms} = \frac{h}{\kappa}\left(\frac{1}{hl}\int_0^l \int_0^h (v_x^2 + v_z^2)\mathrm{dxdz}\right)^{\frac{1}{2}}, \tag{3.6}$$

where v_x and v_z are the components of velocity $\vec{v}$, κ is the thermal diffusivity. This quantity averages the value of the velocity magnitude over the whole domain Ω and is a measure of overall velocity occuring in the domain. The convergence of this quantity to the benchmark target is depicted in the Fig. 3.4 b) and shows that this result is also in line with the benchmark. Both results are also written in the table 3.1.3 together with benchmark parameters (most of the benchmark parameters are omitted because of the use of dimensionless numbers). Parameter θ stands for the parameter in the Crank-Nicolson scheme (for details see section 2.4.1). The results were computed on 80x80 mesh with crossed Taylor-Hood elements (see section 2.4.2).

Quantities	ΔT	Ra	η	T_0	θ	Nu	v_{RMS}
Parameters	1000	10^4	1	0	0.5		
Computed values (mesh 80x80)						4.888	42.8649
Benchmark values (mesh 72x72)						4.884	42.8649

Table 3.1: The comparison of the computed results (blue) with the benchmark values (purple) (in steady state)

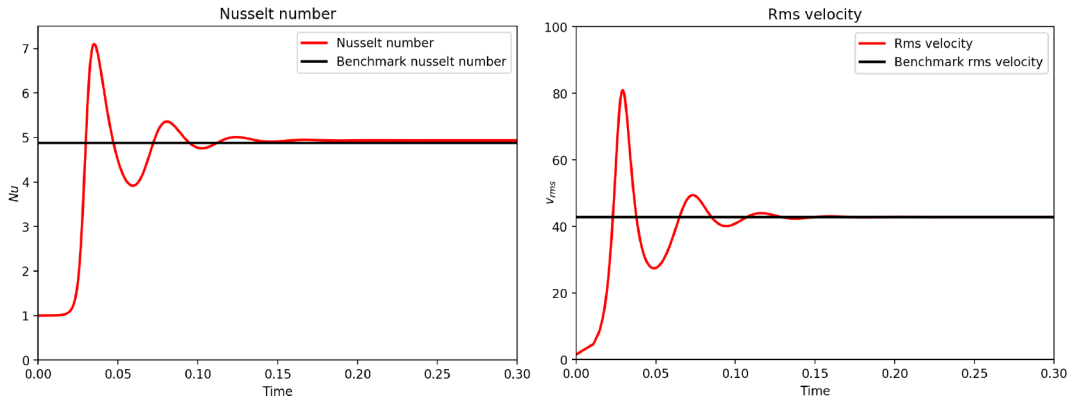

(a) Nusselt number (b) Root mean square velocity

Figure 3.4: Evolution of the velocity field in the thermal convection benchmark

3.2 Free surface benchmark

The process of generation of the chaotic terrains on Europa is linked to the topographical changes of the surface as was introduced in the motivation chapter 1.1. Hence, the numerical simulation of the final application should contain the

framework which enables a movement of the surface based on the domain deformation. This framework can be introduced by assuming almost the same setup as in the Blankenbach benchmark in section 3.1. The difference is in computing with the pressure $p = \pi + p_0$ consisting of both dynamic and hydrodynamic pressures instead of computing solely with π. This change is assumed because of the numerical stability of the problem and it modifies the balance of linear momentum equation by taking 2.56 instead of 2.54 as was discussed in the nondimensionalisation section 2.2.3 as was shown in nondimensionalisation chapter. Moreover, we cannot prescribe the free slip condition at the top boundary Γ_T. The boundary condition of this setup can be written by assuming zero normal component of the deviatoric stress tensor $\boldsymbol{\sigma}$ instead.

3.2.1 Governing equations

The governing equations for this benchmark are analogical to the governing equations for the Blankenbach thermal convection and follow the Boussinesq approximation. The benchmark modifies the balance of linear momentum as was stated above, hence the equations for this benchmark follow the nondimensional equations (2.53),(2.55), and (2.56) as was shown in section regarding nondimensionalisation 2.2.3.

The first equation in the system is the continuity equation

$$\nabla \cdot \vec{v} = 0, \tag{3.7}$$

where $\vec{v}$ is the velocity, This equation is followed by the balance of momentum equation

$$-\frac{Ra}{\alpha \Delta T}\nabla p + \nabla \cdot \boldsymbol{\sigma} + Ra(T - T_0)\vec{e_z} - \frac{Ra}{\alpha \Delta T}\vec{e_z} = \vec{0}, \tag{3.8}$$

which differs to the previous benchmark by not fixing the dynamic pressure in one point of the domain but rather assuming p is the pressure including both the dynamic and the hydrodynamic pressure, Ra is the Rayleigh number, T is the temperature, and T_0 is the reference temperature. The last equation of this system is the heat equation which remains the same as in fixed domain setting.

$$\frac{\partial T}{\partial t} + \vec{v} \cdot \nabla T = \Delta T \tag{3.9}$$

where t is the time. The rheological relationship is again assumed as in Eq. 2.45 following the Newtonian fluid definition.

3.2.2 Problem Geometry

The problem geometry in case of free surface is very similar to the geometry presented for the original Blankenbach thermal convection benchmark. The only change of the setup is in assuming of the free surface boundary condition $\boldsymbol{\sigma} \cdot \vec{n} = \vec{0}$ which ensures the top boundary moves freely according to the stress of the material in the domain. The scheme of the problem geometry of the setup is

depicted in the Fig. 3.5. The other boundary conditions remain the same as in section 3.1 i.e. the side boundaries $\Gamma_L \cup \Gamma_R$ of the domain are assumed to be thermally insulating $\nabla T \cdot \vec{n} = 0$. The contact of the fluid with the boundary is defined by a free slip boundary condition with no inflow and outflow through the boundary $\boldsymbol{\sigma} \cdot \vec{n} = 0$, $\vec{v} \cdot \vec{n} = 0$ which allows the liquid to freely flow without the tension at the boundaries.

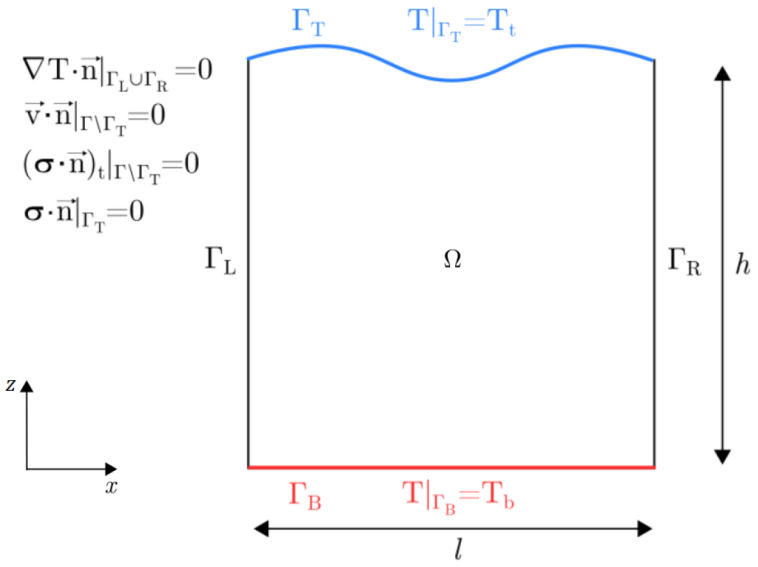

Figure 3.5: The schema of the problem geometry for the free surface thermal convection benchmark

In order to simulate steady state, it is necessary to begin with a non-balanced initial temperature distribution similarly to the previous section 3.1 which is again modelled by a small sinusoidal deviation from the balanced linearly decreasing temperature field given by the following equation

$$T(x, z) = 1 - z + 0.01 \cos(\pi x) \sin(\pi z) \tag{3.10}$$

where the x and z are the spatial coordinates.

3.2.3 Results

The numerical implementation in this benchmark differs significantly from the Blankenbach benchmark where the shape of the domain was fixed. The main difference is in the addition of the evolution equation for the mesh displacement. The points of mesh are initially discretized as crossed Lagrange finite elements of a rectangular shape (for more information see section 2.4.1).

The displacement of the mesh elements was introduced in section 2.3 and is a function denoted as $\hat{\varphi}(\vec{\xi}, t)$ corresponding to mapping from the Arbitrary Lagrangian Eulerian reference frame to the actual configuration. This allows the simulation to move with the mesh grid, and thus simulate the free surface. The simulation uses stabilization mechanism from Kaus et al. [2010] and Nitsche's method following from Juntunen and Stenberg [2009]. These phenomena are described in sections 2.3.3 and 2.3.4 in more detail.

The way how to check the validity of the free surface implementation is to compare the values of thermal convection benchmark in section 3.1 to the topography generated by the free surface.

Dynamic topography is a tool used in geodynamics which evaluates the elevation caused by the flow of the material in the mantle. The dynamic topography is obtained by focusing on the forces acting on the surface. The resulting topography h can be calculated by comparing of normal stress with the hydrostatic pressure

$$\vec{n} \cdot \boldsymbol{\tau} \vec{n} = \rho_0 g_0 h, \tag{3.11}$$

where ρ is the fluid density, g is the magnitude of gravitational acceleration. In two dimensions assuming Newtonian fluid rheology (i.e. Eq. (2.45)), the equation reduces to

$$h = -\frac{\alpha \Delta T}{Ra}(\boldsymbol{\sigma}_{22} - p), \tag{3.12}$$

where $\boldsymbol{\sigma}_{22}$ is a second diagonal element of deviatoric stress tensor $\boldsymbol{\sigma}$ and the fraction $\frac{\alpha \Delta T}{Ra} = \frac{1}{g_0 \rho_0}$.

The free surface benchmark in this section measures the topography directly whereas the fixed domain benchmark in section 3.1 needs to calculate the topography via Eq. (3.12). This has been done for five points at the deformed top boundary and the comparison of results is depicted in the Fig. 3.6. There is a small error in the limit of displacement, which is, however, tolerable as the dynamic topography calculation is only an approximative way which ignores the change of the domain shape. That in turn changes the direction of the normal vector, and thus may slightly increase or lower the result. The change in topography at various point at the top boundary is depicted in the Fig. 3.7.

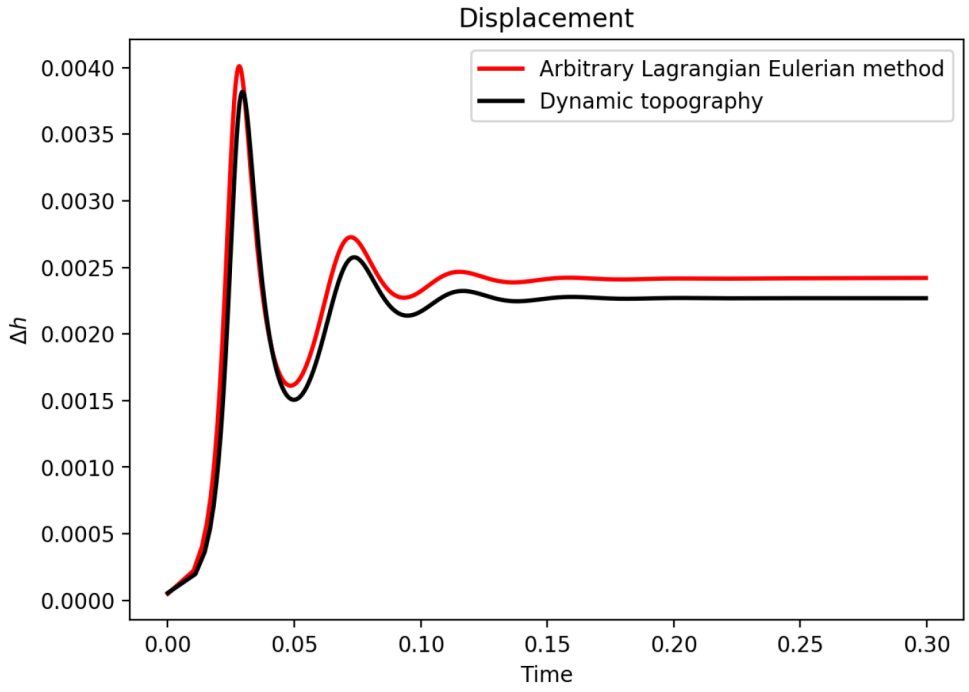

Figure 3.6: The comparison of a topography generated by the deformation of the free surface and the computed dynamic topography from the fixed domain case (at point =(0.0,1.0)

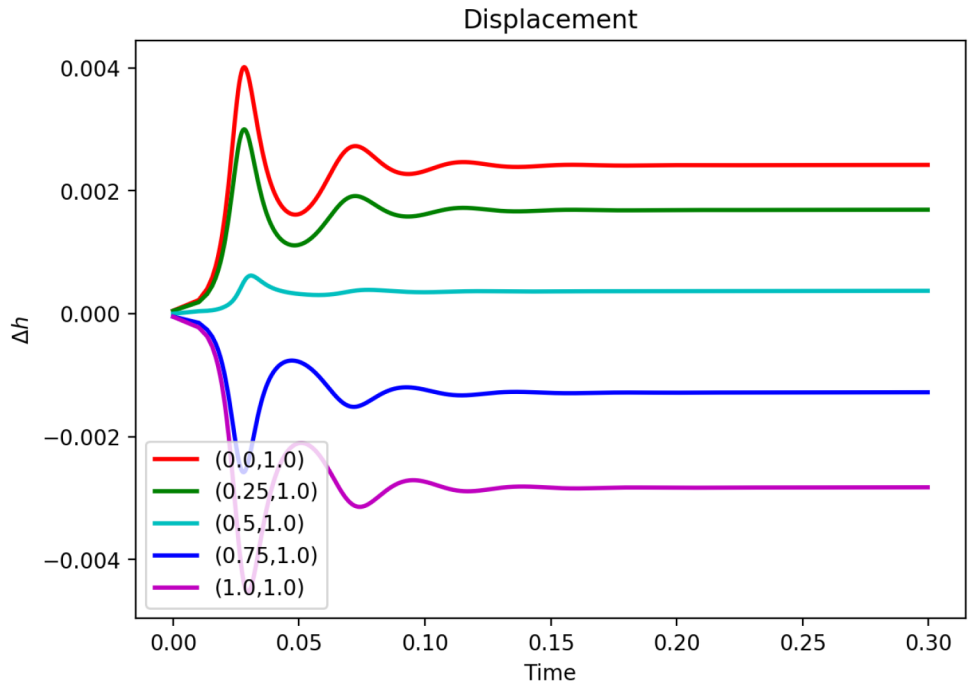

Figure 3.7: The analysis of a topography generated by the deformation of the free surface in five distinct points at the top boundary

3.3 Viscoplastic Thermal Convection Benchmark

This section follows the benchmark by [Tosi et al., 2015] who studied the effect of pseudoplastic rheology on the mobilization of the cold surface material in the problem of the Earth's mantle convection. The setup is very similar to the previously mentioned thermal convection benchmark in chapter 3.1, however, with the added plasticity term in the viscosity definition.

3.3.1 Governing equations

The governing equations corresponding to this test are the equations for Boussinesq convection in a fluid where we take their nondimensional form derived in section 2.2.3. The governing equations for this problem assume constant thermal diffusivity and expansivity and are the same as in Blankenbach benchmark which are reminded for the sake of clarity to the reader as follows

$$\nabla \cdot \vec{v} = 0, \tag{3.1}$$

$$-\nabla p + \nabla \cdot \boldsymbol{\sigma} + Ra(T - T_0)\vec{e}_z = \vec{0}, \tag{3.2}$$

$$\frac{\partial T}{\partial t} + \vec{v} \cdot \nabla T = \Delta T. \tag{3.3}$$

where the first equation is the continuity equation, the second equation is the

balance of linear momentum and the last one is the heat equation (for more details see the derivation in section 2.2.2). The rheological relationship is assumed in a form of Newtonian fluid following the Eq. (2.45) The difference of this benchmark lies in the prescribed effective viscosity which consists of its linear viscous part and its plastic part following the definition in Tosi et al. [2015]

$$\eta(T, z, \dot{\boldsymbol{\epsilon}}) = 2\left(\frac{1}{\eta_v(T, z)} + \frac{1}{\eta_p(\dot{\boldsymbol{\epsilon}})}\right)^{-1}. \tag{3.13}$$

The linear viscous part is given by the linearized Arrhenius law (known also as Frank-Kamenetskii approximation, [Frank-Kamenetskii, 1969])

$$\eta_v(T, z) = \exp(-\gamma_T T + \gamma_z(1 - z)). \tag{3.14}$$

where $\gamma_T = ln(\Delta\eta_T)$ and $\gamma_z = ln(\Delta\eta_z)$ are parameters which control the contrast of the viscosity in temperature and pressure. The non-linear plastic part of the viscosity follows the form in Trompert and Hansen [1998]

$$\eta_p(\dot{\epsilon}) = \eta^* + \frac{\sigma_Y}{\sqrt{\dot{\epsilon} : \dot{\epsilon}}} \tag{3.15}$$

where η^* is the cutoff constant handling the situations where high stresses occur following Stein et al. [2014] and σ_Y is the yield stress which is assumed constant in this benchmark.

3.3.2 Problem geometry

The geometry of the problem is the same as in thermal convection benchmark in section 3.1 and consists of a two-dimensional square box Ω, where the top boundary Γ_T and the bottom boundary Γ_B are continuously cooled and heated, respectively. The side boundaries are considered insulating $\nabla T \cdot \vec{n} = 0$. The benchmark assumes free slip condition $(\boldsymbol{\sigma} \cdot \vec{n})_t = 0$ on boundary Γ and there is no inflow and outflow of the material $\vec{v} \cdot n = 0$. The schema of the domain Ω together with the prescribed boundary conditions is depicted in the figure 3.3.2.

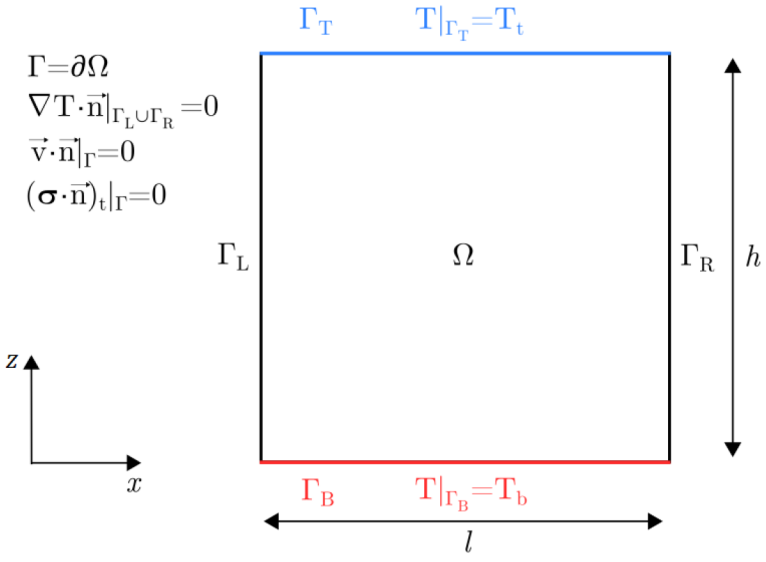

Figure 3.8: The schema of the problem geometry for the viscoplastic thermal convection benchmark

3.3.3 Results

The thesis follows the first two cases of the benchmark tests with the parameters for the individual cases in the following table 3.3.3. Both of the cases assume no depth dependence of the viscosity. The case 2 simulates the plastic part of the deformation by assuming non-zero yield stress σ_Y. This enables the deformation to switch to the plastic regime and increase the plastic part of effective viscosity given by Eq. 3.15. This mobilizes the mantle in the top part of the domain to form a mobile lid of an increased effective viscosity covering part of the region near the top boundary. This as a result increase the velocities near the boundary and the convection mechanism is exchanging the heat with the top boundary whereas the case 1 results in the stagnant lid where the convection mechanism runs deep under the layers of higher viscosity.

Case	*Ra*	$\Delta\eta_T$	$\Delta\eta_z$	η^*	σ_Y
1	10^2	10^5	1	-	-
2	10^2	10^5	1	10^{-3}	1

Table 3.2: The choice of parameters in viscoplastic thermal convection benchmark

The results of the particular simulations are shown in the following table 3.3 where the blue values match the performed simulations in this thesis while the purple values correspond to the benchmark values. The results show the values computed in the thesis are almost in line with the benchmark values which is also supported by the figures depicting scalar fields of the variables evaluated in the tests. The reason why the values slightly differ might be because of our simulation was stopped at time $t = 1.0$ but the quantities might not be in steady state yet or possibly because of different discretization of the problem. In our case 40x40 mesh grid with crossed Taylor-Hood elements (see section 2.4.2) was used. Overall, the results match the benchmark values very well.

Models	$\langle T \rangle$	Nu_{top}	Nu_{bot}	v_{RMS}	v_{RMS}^{surf}	v_{max}^{surf}	η_{min}	η_{max}
Case 1	0.7751	3.5971	3.4127	249.552	1.912	2.622	-	-
Case 2	0.6003	8.7532	8.6391	140.920	103.919	121.234	$1.995{\cdot}10^{-5}$	1.692
Case 1	0.7759	3.5889	3.4231	249.573	1.870	2.607	-	-
Case 2	0.6032	8.7475	8.6440	140.522	104.585	121.696	$1.961{\times}10^{-5}$	1.796

Table 3.3: The comparison of the computed results (blue) with the benchmark values (purple)

The following figure 3.9 depicts the resulting two-dimensional scalar fields for viscosity, temperature and RMS velocity in the steady state of the case 1.

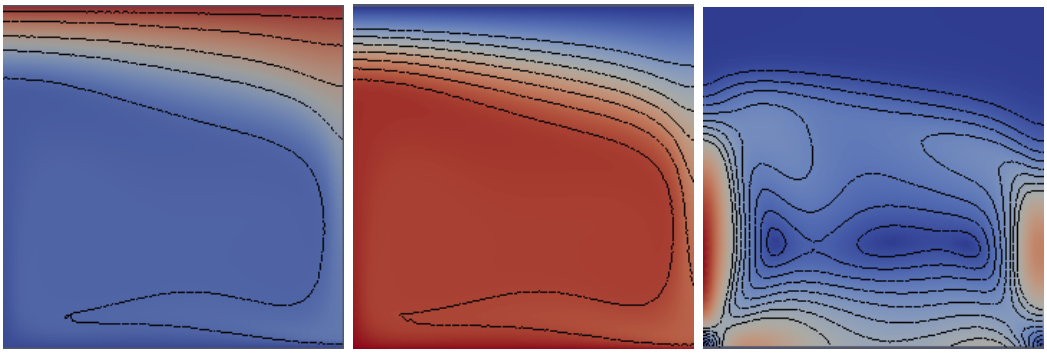

(a) Viscosity (b) Temperature (c) RMS velocity

Figure 3.9: The scalar fields for the steady state of case 1

The figure 3.10 depicts the same quantities as the previous one, however, for the steady state of case 2.

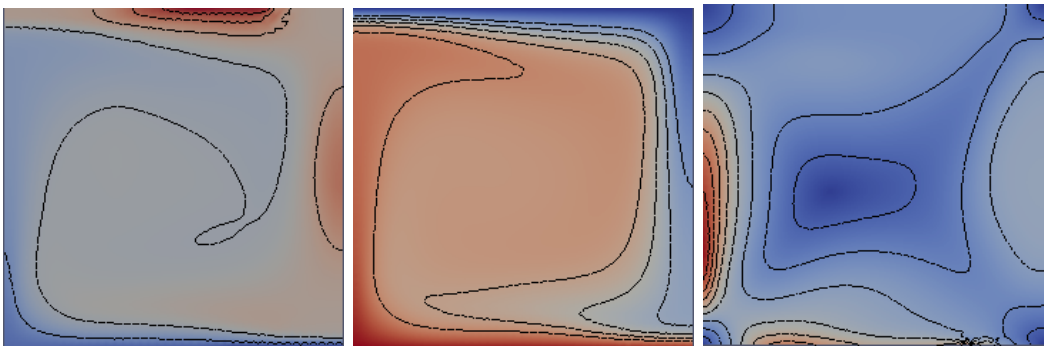

(a) Viscosity (b) Temperature (c) RMS velocity

Figure 3.10: The scalar fields for the steady state of case 2

In contrast to case 1, where plasticity is not considered, the temperature dependence of viscosity leads to the formation of highly viscous immobile (stagnant) lid (reddish color at the surface of computational domain in Fig. 3.10 (a)). The reduction of viscosity which has was included through the plastification of the material at the surface leads to breaking of the stagnant lid and mobilization of the top surface. This behavior is often used in models of thermal convection in the Earth's mantle where it mimics the plate tectonics behavior. [Tosi et al., 2015]

The results are in line with the benchmark values which is compared in the following Fig. 3.11 which compares the temperature, viscosity and root mean square velocity fields computed in the thesis (right) and in the benchmark (left). Similarly, the same quantities are compared also for the case 2 in Fig. 3.12.

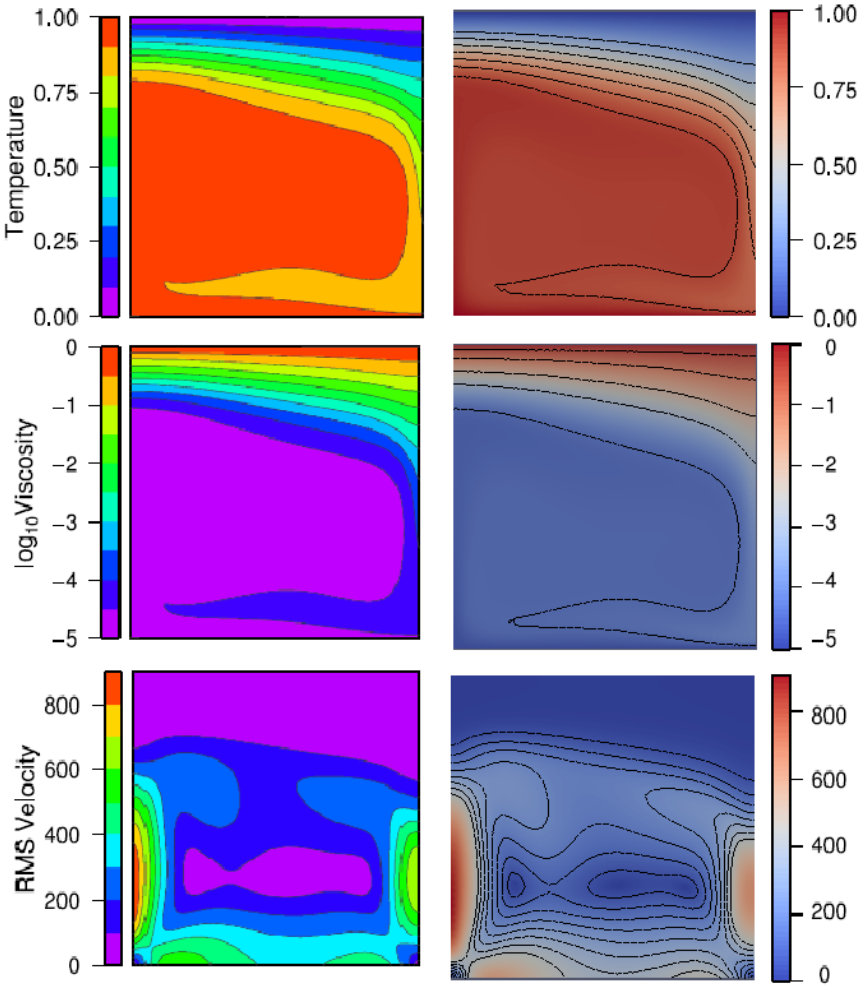

Figure 3.11: The comparison of simulated scalar quantities (right) with the benchmark values from Tosi et al. [2015] (left) in case 1

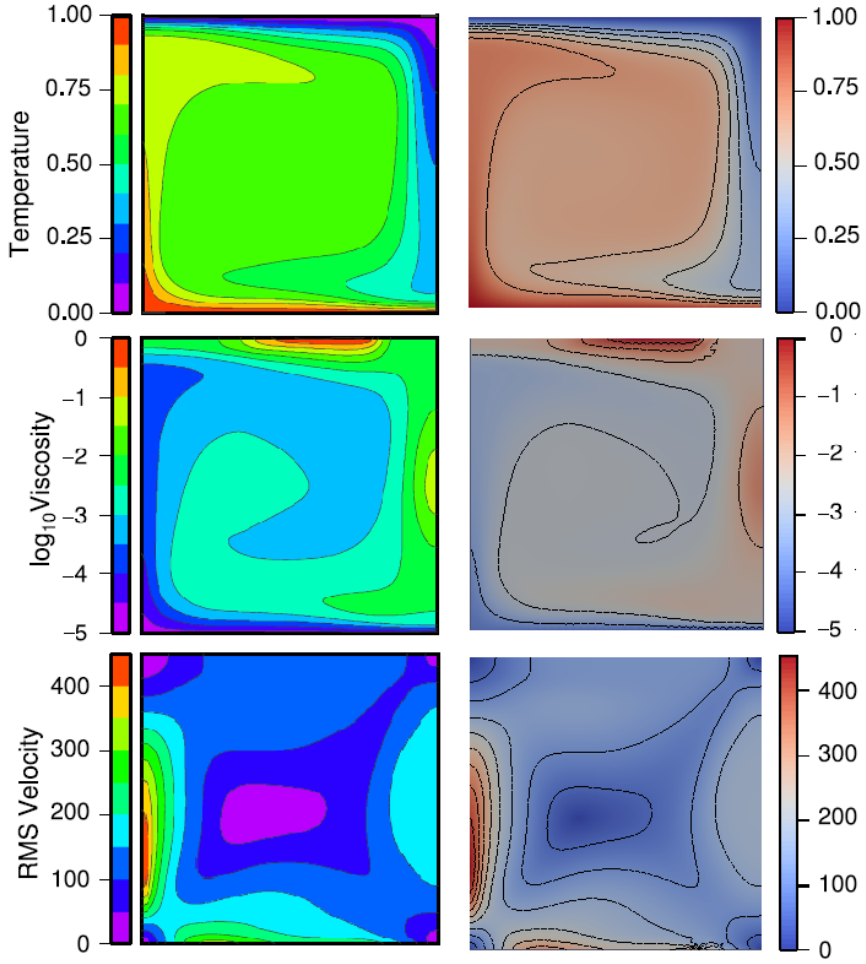

Figure 3.12: The comparison of simulated scalar quantities (right) with the benchmark values from Tosi et al. [2015] (left) in case 2

Figures 3.13 and 3.14 show the depth profiles of horizontally-averaged quantities (temperature T, viscosity η, rms velocity v_{RMS}). Comparison of our results (left column) with the results from Tosi et al., 2015 (right column) shows a good agreement.

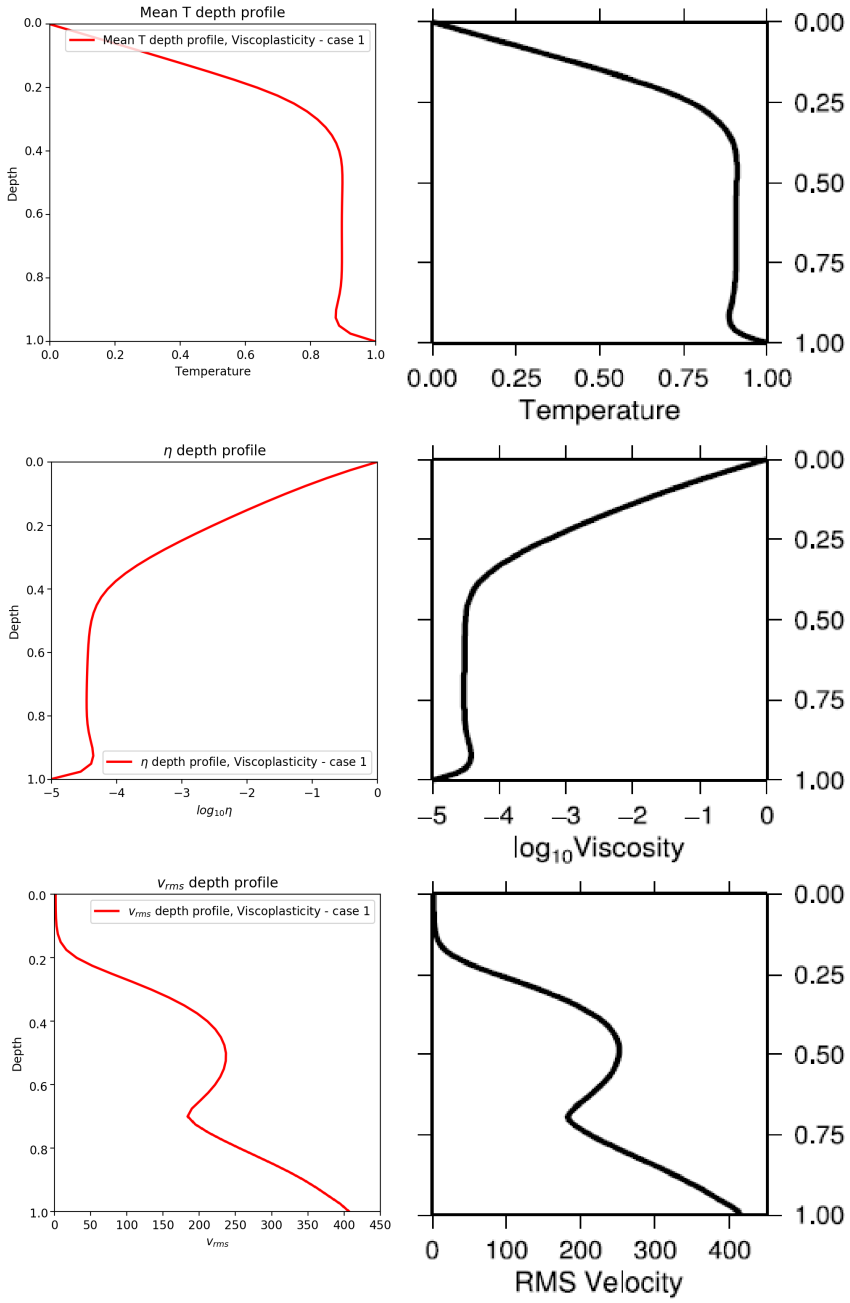

Figure 3.13: The comparison of simulated depth profile of temperature, viscosity, and RMS velocity (left) with the benchmark values from Tosi et al. [2015] (right) for the steady state of case 1

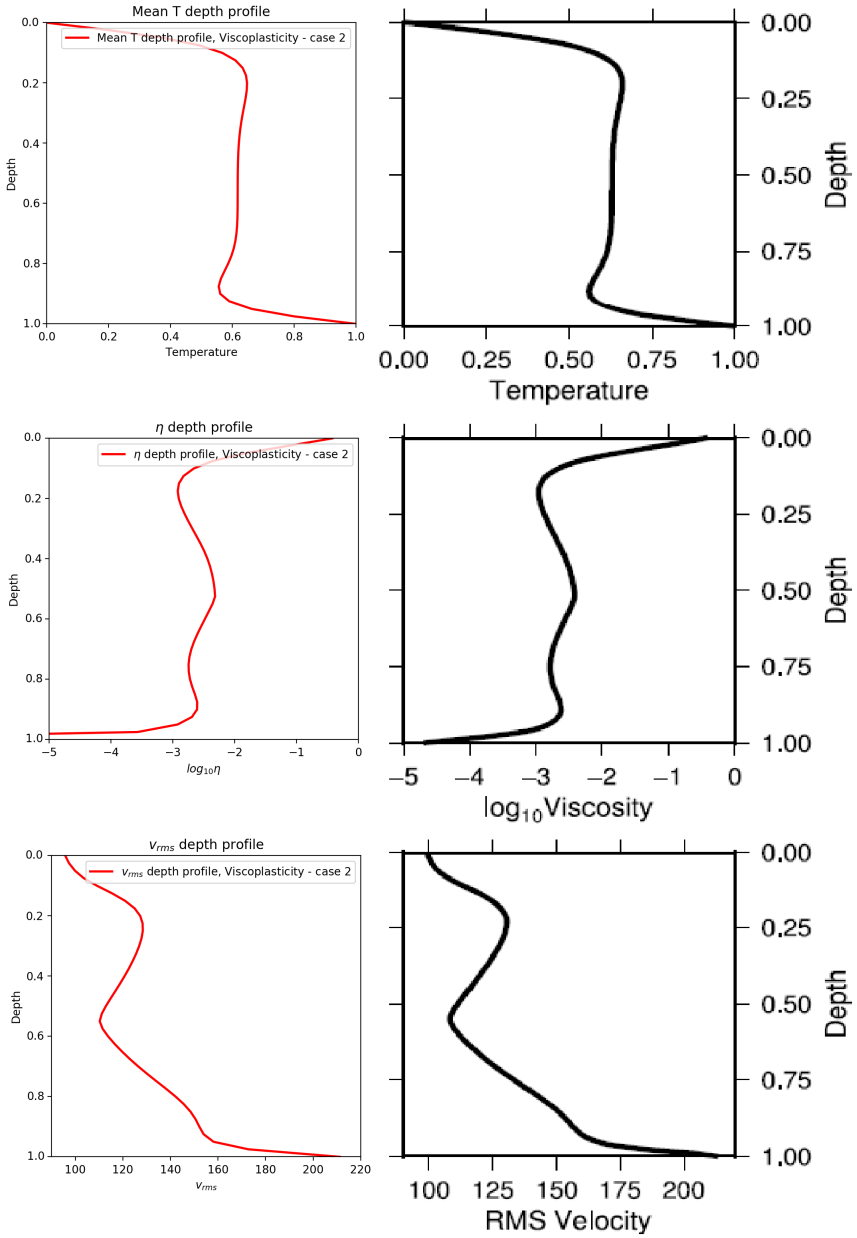

Figure 3.14: The comparison of simulated depth profile of temperature, viscosity, and RMS velocity (left) with the benchmark values from Tosi et al. [2015] (right) for the steady state of case 2

3.4 Shear Bands Benchmark

The following section follows the dissertation thesis by Maierová [2012] who ran a series of simulations regarding the strain weakening effect, which is a necessary feature for the modelling of the plastic failure of the Europa's surface in the chaotic terrains formation. The strain weakening as a phenomenon is described in more detail in 2.2.4 where is also the derivation of the corresponding functions for $C = C(\epsilon_p^{II})$ and $\sigma_Y = \sigma_Y(p, C, \varphi)$, where φ is the angle of internal friction.

As a benchmark for the strain weakening effect, the thesis follows the setup from the dissertation thesis of Maierová [2012]. This approach slightly modified and simplified the setup from Lemiale et al. [2008] and Kaus [2010] who studied the initiation of shear bands in geodynamical numerical models of brittle deformation.

3.4.1 Governing equations

The governing equations for this problem consist of the Stokes problem coupled with the evolution of plastic strain $_p$

The first equation in the solved system is the continuity equation

$$\nabla \cdot \vec{v} = 0, \tag{3.16}$$

where $\vec{v}$ is the velocity. The equation is followed by the balance of momentum equation

$$-\nabla p + \nabla \cdot \boldsymbol{\sigma} + \rho \vec{g} = \vec{0}, \tag{3.17}$$

where g is the gravity acceleration, ρ is the density of the ice and $\boldsymbol{\sigma}$ is the stress tensor defined for Newtonian fluids as in Eq. (2.45) i.e. $\boldsymbol{\sigma} = 2\eta_{eff}\dot{\boldsymbol{\epsilon}}$. The last equation of this system is the plastic strain advection equation

$$\frac{\partial \epsilon_p^{II}}{\partial t} + \vec{v} \cdot \nabla \epsilon_p^{II} = \dot{\boldsymbol{\epsilon}}_p^{II} \tag{3.18}$$

where $\boldsymbol{\epsilon}_p$ is the plastic strain, and the superscript $(\cdot)^{II}$ denotes second invariant as defined in section 2.1. The effective viscosity η_{eff} is defined as

$$\eta_{eff} = \left(\frac{1}{\eta_v} + \frac{1}{\eta_p} \right)^{-1}. \tag{3.19}$$

which was obtained from the relation that sum of $\dot{\boldsymbol{\epsilon}}_p + \dot{\boldsymbol{\epsilon}}_v = \dot{\boldsymbol{\epsilon}}$ and the following equation

$$\boldsymbol{\sigma} = 2\eta_{eff}\dot{\boldsymbol{\epsilon}} = 2\eta_v\dot{\boldsymbol{\epsilon}}_v = 2\eta_p\dot{\boldsymbol{\epsilon}}_p \tag{3.20}$$

In the viscous regime, a constant dimensionless viscosity $\eta_v = 10^5$ is prescribed everywhere except for the small weak inclusion at the bottom boundary where the viscosity is $\eta_v = 1$. This weak inclusion starts the failure of the material and thus initiate the shear bands. In the plastic regime, the viscosity is given by

$$\eta_p = \frac{\sigma_Y(p, C, \varphi)}{2\dot{\boldsymbol{\epsilon}}^{II}(\vec{v})} \tag{3.21}$$

where the functional forms of the cohesion C and σ_Y follows the definitions from section 2.2.4 enabling the strain weakening effect in the material. This gives us

$$\eta_{eff} = \left(\frac{1}{\eta_v} + \frac{2\dot{\boldsymbol{\epsilon}}^{II}(\vec{v})}{\sigma_Y(p, C, \varphi)} \right)^{-1}. \tag{3.22}$$

3.4.2 Problem geometry

The problem setup assumes rectangular geometry with the width four times larger than height of the domain Ω. There is a free surface $\boldsymbol{\sigma} \cdot \vec{n} = 0$ at the top boundary and free slip $(\boldsymbol{\sigma} \cdot \vec{n})_t = 0$ on $\Gamma_R \cup \Gamma_B \cup \Gamma_R$. The no inflow/outflow condition $\vec{v} \cdot \vec{n} = 0$ is prescribed at Γ_B and inflow of magnitude $v_x = x$ on Γ_L and inflow of magnitude $v_x = -x$ on Γ_R.

The 0.04×0.02 region in the middle of bottom boundary is assumed to have a weak inclusion in a viscosity assuming $\eta_v = 1$ in the region and $\eta_v = 10^5$ elsewhere. The problem geometry is depicted in the schema 3.15 from Maierová [2012].

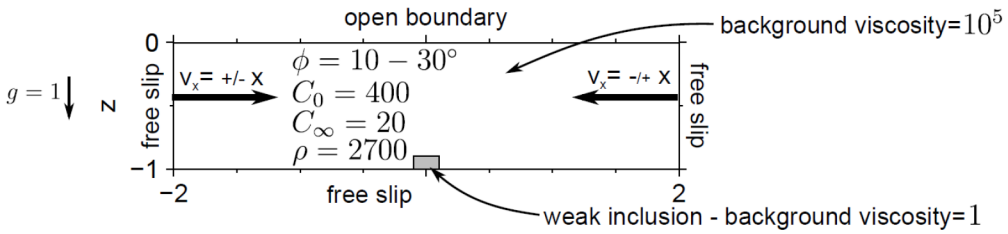

Figure 3.15: The schema of the problem geometry for the strain weakening benchmark

Source: Maierová [2012]

The numerical discretization of the simulations for which we compute the results follow the choice done by Maierová [2012], and thus the resolution of the simulation is 400x100 elements with the crossed rectangular Taylor-Hood elements for Stokes problem, which is described in section 2.4.2, and discontinuous Galerkin elements of degree 0 for $\boldsymbol{\epsilon}_p$, which is described in section 2.4.4.

3.4.3 Results

In the following figure 3.16, we plot the strain rate in a simulation of the initiation of the shear bands by compression of the domain with a prescribed velocity generating the inflow of material at the side boundaries $\Gamma_R \cup \Gamma_L$. The respective figures show the strain rate at time $t = 0.0005$ which corresponds to the 0.5% shortening of the domain. Three scenarios were computed for the problem where the friction angle $\varphi \in \{\pi/18, \pi/9, \pi/6\}$.

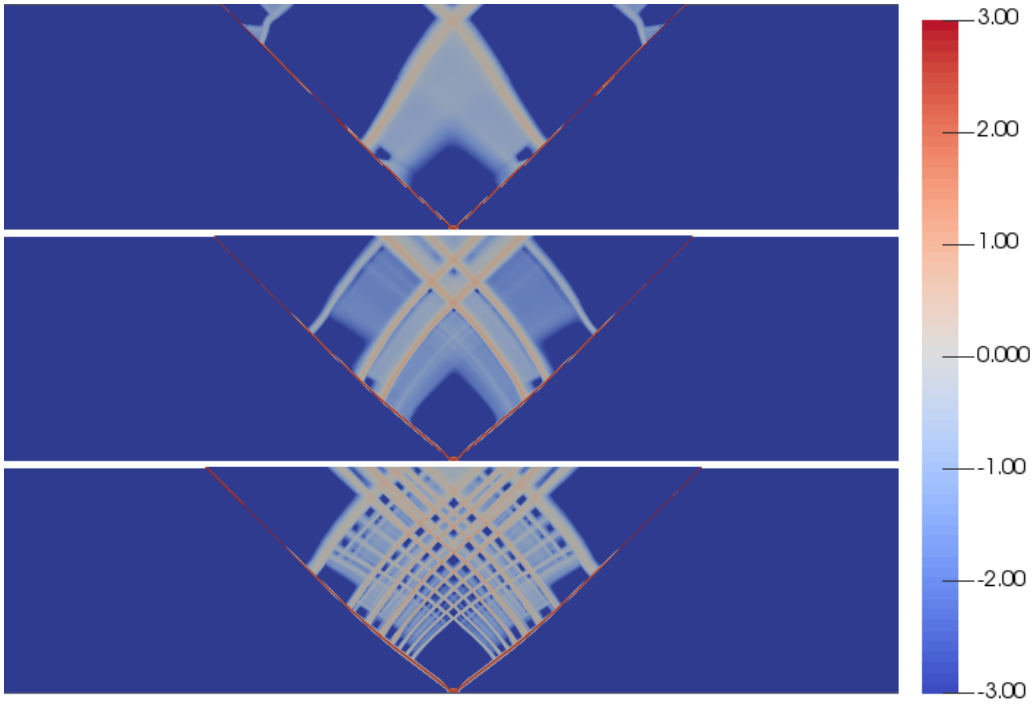

Figure 3.16: Initiation of shear bands for compression by inflowing material for different internal friction angles: $\phi = \pi/18$ (top), $\phi = \pi/9$ (middle), $\phi = \pi/6$ (bottom)

The figure depicts three scenarios of material inflow in the rectangular domain which represents a planetary body mantle where an effect of strain weakening allows for the cracking of the material in the domain. At the point of when the domain has gone through 0.5% shortening, the main shear bands (which emerged due to the weak inclusion in viscosity) exhibit a formation of the secondary shear bands. With the increase of the angle of internal friction the production of the secondary shear bands seems more active from the results obtained in Fig. 3.16.

The angle between the main stress axis and the shear bands should depend on the angle of internal friction by having roughly between $\frac{\pi}{4}$ (Roscoe angle) and $\beta(\phi) = \frac{\pi}{4} - \frac{\phi}{2}$ (Coulomb angle) tilt. [Lemiale et al., 2008]

The simulations ran by Kaus [2010] or Maierová [2012] show the higher resolution gets closer to the Coulomb angle and lower resolution got closer to the Roscoe angle.

This, however, holds in our simulation only approximately as we obtained values of the Coulomb angle $\beta(10°) \doteq 43.2°$, $\beta(20°) \doteq 40.7°$, $\beta(30°) \doteq 37.9$ for the respective angles. The theoretical values corresponding to these angles of internal friction should, however, be 40°, 35°, 30°, respectively. The correction of this might be by assuming stabilization of the pressure overshoot near the shear band as was done in Maierová [2012] or increase of the numerical resolution.

4. Results and discussion

This chapter presents the results of the final problem defined in section 2.1 and discusses the results of all benchmarks and the final application to Europa. The setup applied to Europa is rather experimental i.e. the model is considered as outlook which might be made more accurate in the possible future extensions.

4.1 Application to Europa

In order to simulate the mechanism on Europa, three preliminary setups of simulations were run with simplified parameters and one with the fully specified final application (Case 4).

The numerical methods used to model this problem were discussed in 2.4 including the choice of Taylor-Hood elements for the Stokes problem, Picard iterations to handle the non-linearity, ALE method to treat the free surface, and discontinuous Galerkin elements in order to model the advection equation for plastic strain rate (2.3).

The model was not specified and thus several different setups were launched as a test in order to find out what parameters that correspond to the real Europa parameters might be reasonable to assume in the model. The summary of parameters for the individual simulations can be found in 4.1.

The case 1 is the most simple setup, which had a goal to test only the melting process in the domain which is a mechanism which was previously used e.g. in Kalousová et al. [2016], however, there is no plasticity, and thus there is no observable cracking in the model and the volume is diminishing purely viscously.

The case 2 is a similar setup but there is a plastic regime in which is the yield stress supposed constant along the whole domain Ω. This model seems as more hopeful scenario than case 1, however, there is missing the phenomenon of strain weakening introduced in 2.2.4.

In order to fix this, we run case 3 and 4 where in the former there is yield stress dependent on the pressure and cohesion, where the cohesion is assumed constant, and in the case 4, the setup is complete with strain weakening property given by Eq. (2.62) which is included in the model.

Case	η_v $[Pa \cdot s]$	η_p $[Pa \cdot s]$	σ_Y $[Pa]$	C $[Pa]$
1	10^{18}	-	-	-
2	10^{24}	$\eta_p(\sigma_Y, \dot{\boldsymbol{\epsilon}})$	10^6	-
3	10^{24}	$\eta_p(\sigma_Y, \dot{\boldsymbol{\epsilon}})$	$\sigma_Y(p, C, \phi)$	10^6
4	$\eta_v(T)$	$\eta_p(\sigma_Y, \dot{\boldsymbol{\epsilon}})$	$\sigma_Y(p, C, \phi)$	$\mathrm{C}(\boldsymbol{\epsilon}_p^{II})$
Other parameters		Value		Units
h		30000		m
l		60000		m
x_0		30000		m
z_0		60000		m
Δx		30000		m
Δz		60000		m
γ_0		10^{-10}		$kg \cdot m^{-3} \cdot s^{-1}$
σ_{min}		0.1		Pa
C_0		10^5		Pa
C_∞		10^4		Pa
ϵ_0		0.0		s^{-1}
ϵ_∞		0.1		s^{-1}
g		1.32		$m \cdot s^{-2}$
ϕ		30ř		$^\circ$
ρ_{ice}		920		$kg \cdot m^{-3}$
ρ_{water}		1000		$kg \cdot m^{-3}$
T_0		270		K
T_{min}		100		K
T_{max}		270		K
T_{region}		230		K
η_0		10^{16}		$Pa \cdot s$
Q		$5{\cdot}10^4$		$J \cdot mol^{-1}$
R		8.314		$J \cdot K^{-1} \cdot mol^{-1}$

Table 4.1: The choice of parameters in final application on Europa simulations

A simulation was run for each case and the Figs. 4.1, 4.2, and 4.3 depict the evolution of strain rate $\dot{\boldsymbol{\epsilon}}$ based on the volumetric decrease in the domain which is governed by parameter γ.

The more focus on the evolution of the case 4 is put in the Fig. 4.4, where all four subfigures relate to the main application.

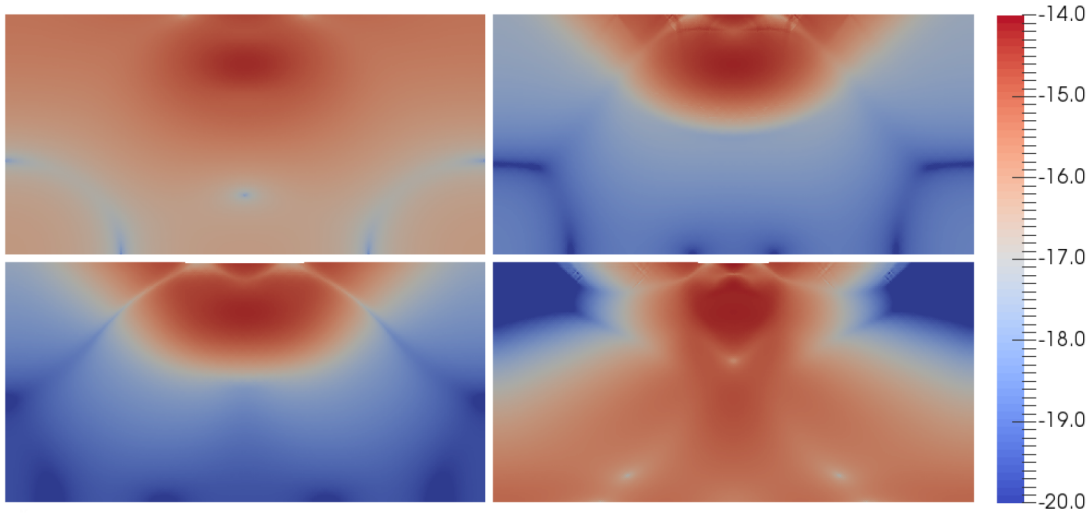

Figure 4.1: The simulation of Europa - Strain rate $\log_{10} \dot{\boldsymbol{\epsilon}}^{II}$ in time $t = 0.13 Myr$ (Case 1 - top, left), (Case 2 - bottom, left), (Case 3 - top, right), (Case 4 - bottom, right)

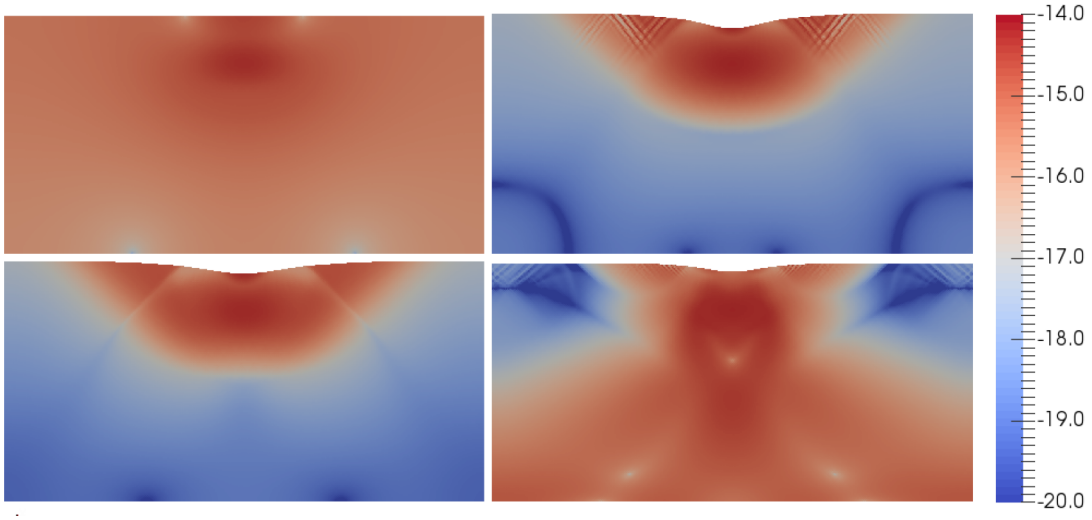

Figure 4.2: The simulation of Europa - Strain rate $\log_{10} \dot{\boldsymbol{\epsilon}}^{II}$ in time $t = 1.60 Myr$ (Case 1 - top, left), (Case 2 - bottom, left), (Case 3 - top, right), (Case 4 - bottom, right)

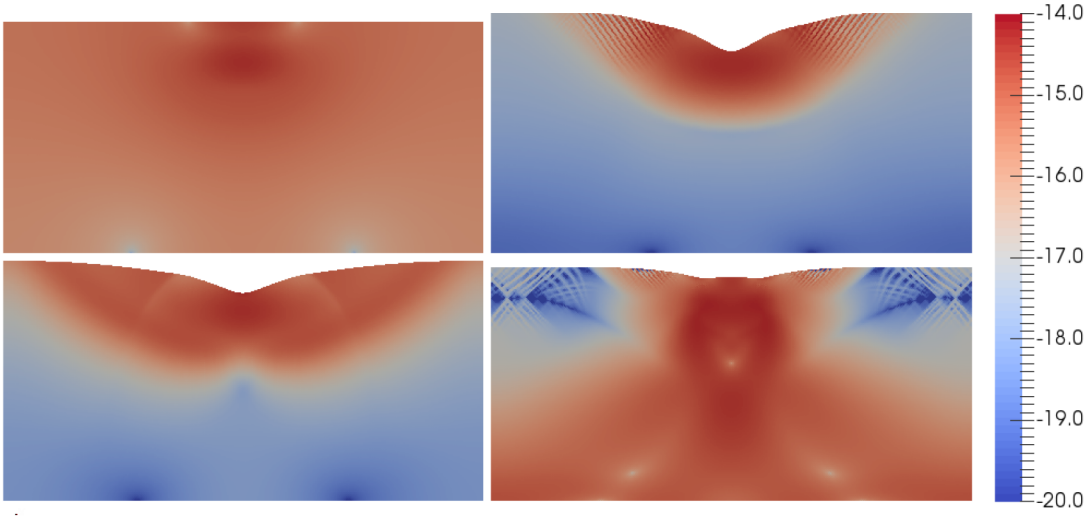

Figure 4.3: The simulation of Europa - Strain rate $\log_{10} \dot{\boldsymbol{\epsilon}}^{II}$ in time $t = 4.70Myr$ (Case 1 - top, left), (Case 2 - bottom, left), (Case 3 - top, right), (Case 4 - bottom, right)

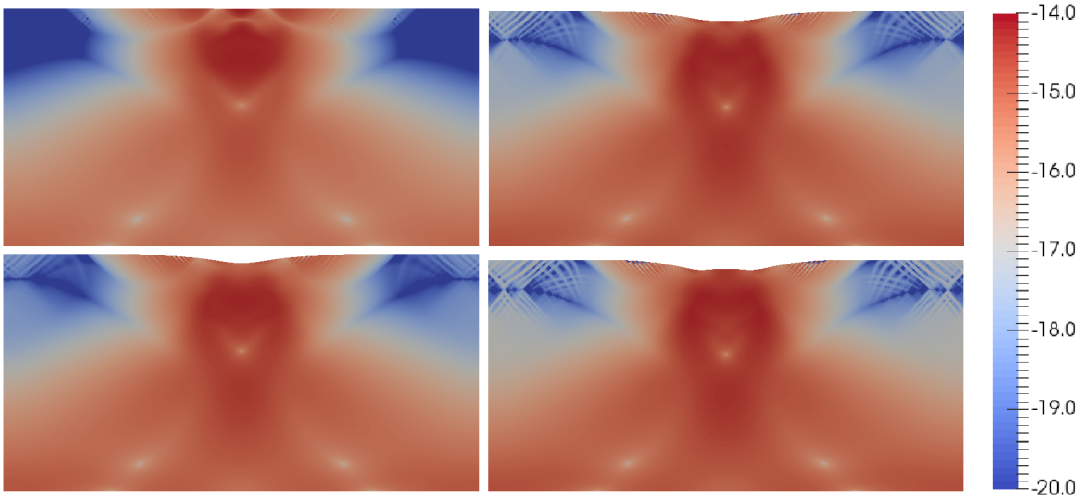

Figure 4.4: The simulation of Europa - Strain rate $\log_{10} \dot{\boldsymbol{\epsilon}}^{II}$ for Case 4. ($t = 0.13Myr$ - top, left), ($t = 1.70Myr$ - bottom, left), ($t = 2.87Myr$ - top, right), ($t = 4.70Myr$ - bottom, right)

The figures show, that the case 1, where there is no plastic regime, does not show any interesting phenomenon except for the melt of the material in the molten region, which causes decrease in the overall volume of the domain.

The case 2 enables the surface to deform with the strain rate dominantly decreasing the topography at the middle of the domain above the water lens. This is a desirable property, as it mimic the lens collapse hypothesis suggested by Schmidt et al. [2011], however, the setup operates dominantly in the viscous regime.

In order to simulate the plastic regime, the yield stress σ_Y is supposed not

spatially constant in the case 3, nevertheless with the constant cohesion C. This setup seems in the inital steps of the simulation similarly to case 2, however, the change in the setup generated a striped region in the Fig. 4.3, which might signalize the shear bands occurence.

The case 4, in contrast, assumes even the presence of the strain weakening phenomenon. The parameters are chosen so that they match other research papers (following the parameters from Kalousová et al. [2016] and viscosity functional form from Showman and Han [2004]). The setup does not generate so clearly noticeable shear bands as the setup in case 3, however, there is a noticeable deformation of the surface near the surface e.g. at Fig. 4.3. An interesting phenomenon is occuring in the regions close to Γ_R and Γ_L near the free surface, where there are emerging shear bands probably due to the strain weakening in the area beneath the surface. A detailed image is depicted in 4.4.

4.2 Discussion

The thesis discussed the results for each benchmark and the final application individually, this discussion summarizes the overall progress throughout the thesis.

The goal of the thesis was to run a series of simulations which should have validated the use of the numerical tools that are necessary in order to model a complex phenomenon such as the chaotic terrains formation. The thesis started with simulation of the thermal convection benchmark which was supposed to set up the course for exploration of more complex tools.

The thermal convection started with the modelling of the decoupled system which combines the Stokes problem with the heat equation and the boussinesq approximation and nondimensionalisation, which enabled us to neglect the nonlinearities and rather build a model on which more complex properties could be modelled.

The implementation of the benchmark by Blankenbach et al. [1989] considered Taylor-Hood elements for the Stokes problem and piecewise quadratic polynomial elements for the heat equation. Moreover, the Crank-Nicolson scheme was used in order to obtain more stable solution for the heat equation.

Next step was to introduce the notion of free surface, which was implemented by constructing of the Arbitrary Lagrangian Eulerian method for the displacement of the mesh nodes. This method requires to handle some of the numerical problems which is the stability problem discussed in 2.3.3. Moreover, the movement of the mesh required to set up the boundary conditions so that they are covered in the weak formulation of the problem which was discussed in the section 2.3.4. When the implementation of the free surface was done, the thesis ran a benchmark to the previously studied thermal convection in a fixed domain. The benchmark compared the values of dynamic topography generated by the forces on the surface Γ_T. This was compared to the generated topography using the mesh displacement and the results were in a good agreement.

The next complexity to the model was added with the introduction of viscoplasticity assuming the material flowing in the domain might switch to the plastic regime where the deformation would proceed differently. This was implemented and checked in comparison to benchmark by Tosi et al. [2015]. In the

end, the effect that was sought is the strain weakening, which enabled the model to cause brittle failure of the crustal material in the domain.

The introduction of the strain weakening was linked to benchmarking of the model in this thesis against the model made by Maierová [2012]. This led to the introduction of discontinuous Galerkin elements in the implementation and a specification of the deformation in the plastic regime followed that.

Last but not least, the setup mimicking the parameters of Jupiter's moon Europa was created. This setup showed that the tools used in this thesis were able to model the behaviour which could theoretically explain the formation of the chaotic terrains by the four phase lens collapse model introduced by Schmidt et al. [2011].

The models used in the thesis, however, faced a lot of assumptions, specially the boussinesq approximation imposed a lot of conditions on the behaviour of the studied system. The thesis also omitted the transfer of heat in the final application which might play a significant role in the evolution of deformations near the surface. On one hand, this approximation enabled us to build and implement a model which would be much harder to create due to nonlinearities if the approximation was not done. On the other hand, as the model gets more and more complicated, the model might suffer either from misspecification due to too many assumptions, or it might lose the connection to the real application.

Conclusion

The Galileo and Cassini missions to the moons of Jupiter and Saturn led to a discovery of fascinating details about some of these icy worlds. One of these worlds is Europa, the Jupiter's moon, which might harbour life in its subsurface oceans. The possibility of presence of life forms led scientists focus more on the understanding of the geodynamical properties of this planetary body.

This thesis focused on the study of the formation process of the so called chaotic terrains. These formations which alternate the Europa's surface might be a result of a complicated geophysical process in the Europa's icy shell. The thesis followed a model assuming the existence of an underwater lake containing water or ice close to the melting state. This model is expected by the research community to answer the fundamental questions about the chaotic terrains formation and the processes running in the Europa's shell.

Several simulations were run in the thesis in order to validate the mentioned mathematical model. These benchmarks were summarized in the discussion chapter and were followed by a construction of an experimental model which suggested, that the mechanisms implemented in the model might be sufficient to model the chaotic terrain formation. Nevertheless, the tools used were limited and the resulting model is rather an outlook of what can be studied more rigorously than a rigorously validated model.

The outlook of this thesis might be to extend the models used in this thesis by experimenting and adding more setups to the final application, or possibly by generalizing of the . setup by adding of the heat equation or extending the model to three spatial dimensions.

Bibliography

Daniel Arndt. Augmented taylor-hood elements for incompressible flow. Master's thesis, Georg-August-Universitität Göttingen, 2013.

B. Blankenbach et al. A benchmark comparison for mantle convection codes. *Geophysical Journal International*, 98(1):23–38, 1989.

Bart Bos and Christopher J. Spiers. Frictional-viscous flow of phyllosilicate-bearing fault rock: Microphysical model and implications for crustal strength profiles. *Journal of Geophysical Research: Solid Earth*, 107(B2):ECV–1, 2002.

Geoffrey Collins and Francis Nimmo. Chaotic terrain on europa. In *Europa*, pages 259–281. University of Arizona Press Tucson, 2009.

Ronadh Cox et al. Is chaos on europa caused by crust-penetrating impacts? In *36th Annual Lunar and Planetary Science Conference*, volume 36, 2005.

John Crank and Phyllis Nicolson. A practical method for numerical evaluation of solutions of partial differential equations of the heat-conduction type. In *Mathematical Proceedings of the Cambridge Philosophical Society*, volume 43, pages 50–67. Cambridge University Press, 1947.

Daniele A. Di Pietro et al. Mass preserving finite element implementations of the level set method. *Applied Numerical Mathematics*, 56(9):1179–1195, 2006.

Jean Donea et al. An arbitrary lagrangian-eulerian finite element method for transient dynamic fluid-structure interactions. *Computer methods in applied mechanics and engineering*, 33(1-3):689–723, 1982.

David A. Frank-Kamenetskii. Mass and heat transfer in chemical kinetics. *Plenum Press, New York*, 1969.

Taras Gerya. Dynamical instability produces transform faults at mid-ocean ridges. *Science*, 329(5995):1047–1050, 2010.

Jason C Goodman et al. Hydrothermal plume dynamics on europa: Implications for chaos formation. *Journal of Geophysical Research: Planets*, 109(E3), 2004.

Mika Juntunen and Rolf Stenberg. Nitsche's method for general boundary conditions. *Mathematics of computation*, 78(267):1353–1374, 2009.

Klára Kalousová et al. Water generation and transport below europa's strike-slip faults. *Journal of Geophysical Research: Planets*, 121(12):2444–2462, 2016.

Boris J.P. Kaus. Factors that control the angle of shear bands in geodynamic numerical models of brittle deformation. *Tectonophysics*, 484(1-4):36–47, 2010.

Boris J.P. Kaus et al. A stabilization algorithm for geodynamic numerical simulations with a free surface. *Physics of the Earth and Planetary Interiors*, 181 (1-2):12–20, 2010.

Vincent Lemiale et al. Shear banding analysis of plastic models formulated for incompressible viscous flows. *Physics of the Earth and Planetary Interiors*, 171 (1-4):177–186, 2008.

Anders Logg et al. *Automated solution of differential equations by the finite element method: The FEniCS book*, volume 84. Springer Science & Business Media, 2012.

Baerbel K. Lucchitta and Laurence A. Soderblom. The geology of europa. In *Satellites of Jupiter*, pages 521–555, 1982.

Petra Maierová. *Evolution of the Bohemian Massif: Insights from numerical modelling*. PhD thesis, Charles University in Prague, 2012.

M. C. Malin and D. C. Pieri. Europa. In J.A. Burns and M.S. Matthews, editors, *Satellites*, pages 689–717. University of Arizona Press, Tucson, 1986.

Michael Manga and C.-Y. Wang. Pressurized oceans and the eruption of liquid water on europa and enceladus. *Geophysical Research Letters*, 34(7), 2007.

Zdeněk Martinec. Continuum mechanics. lecture notes. http://geo.mff.cuni.cz/vyuka/Martinec-ContinuumMechanics.pdf, 2003. [Online; accessed 14-July-2019].

Ctirad Matyska. Mathematical introduction to geothermics and geodynamics. lecture notes. http://geo.mff.cuni.cz/ cm/geoterm.pdf/, 2005. [Online; accessed 14-July-2019].

Loïc Mével and Eric Mercier. Large-scale doming on europa: a model of formation of thera macula. *Planetary and Space Science*, 55(7-8):915–927, 2007.

Giorgio Ranalli. *Rheology of the Earth*. Springer Science & Business Media, 1995.

Britney E. Schmidt et al. Active formation of 'chaos terrain'over shallow subsurface water on europa. *Nature*, 479(7374):502, 2011.

Guus Segal and Kees Vuik. *A simple iterative linear solver for the 3D incompressible Navier-Stokes equations discretized by the finite element method*. Delft University of Technology, Faculty of Technical Mathematics and Informatics, 1995.

Adam P. Showman and Lijie Han. Numerical simulations of convection in europa's ice shell: Implications for surface features. *Journal of Geophysical Research: Planets*, 109(E1), 2004.

Jean-François Sigrist. *Fluid-structure interaction: an introduction to finite element coupling*. John Wiley & Sons, 2015.

Claudia Stein et al. A comparison of mantle convection models featuring plates. *Geochemistry, Geophysics, Geosystems*, 15(6):2689–2698, 2014.

Cedric Taylor and Paul Hood. A numerical solution of the navier-stokes equations using the finite element technique. *Computers & Fluids*, 1(1):73–100, 1973.

Nicola Tosi et al. A community benchmark for viscoplastic thermal convection in a 2-d square box. *Geochemistry, Geophysics, Geosystems*, 16(7):2175–2196, 2015.

Ron Trompert and Ulrich Hansen. Mantle convection simulations with rheologies that generate plate-like behaviour. *Nature*, 395(6703):686, 1998.

Kevin K. Williams and Ronald Greeley. Estimates of ice thickness in the conamara chaos region of europa. *Geophysical research letters*, 25(23):4273–4276, 1998.

List of Figures

List of Tables

List of Abbreviations

- ALE - Arbitrary Lagrangian Eulerian
- JPL - Jet Propulsion Laboratory
- NASA - National Aeronautics and Space Administration